

Scar-induced imbalance in staggered Rydberg ladders

Mainak Pal,¹ Madhumita Sarkar,² K. Sengupta,¹ and Arnab Sen¹

¹*School of Physical Sciences, Indian Association for the Cultivation of Science, Kolkata 700032, India*

²*Department of Physics and Astronomy, University of Exeter, Stocker Road, Exeter EX4 4QL, United Kingdom*

(Dated: December 4, 2024)

We demonstrate that the kinematically-constrained model of Rydberg atoms on a two-leg ladder with staggered detuning, $\Delta \in [0, 1]$, has quantum many-body scars (QMBS) in its spectrum and represents a non-perturbative generalization of the paradigmatic PXP model defined on a chain. We show that these QMBS result in coherent many-body revivals and site-dependent magnetization dynamics for both Néel and Rydberg vacuum initial states around $\Delta = 1$. The latter feature leads to eigenstate thermalization hypothesis (ETH)-violating finite imbalance at long times in a disorder-free system. This is further demonstrated by constructing appropriate local imbalance operators that display nonzero long-time averages for Néel and vacuum initial states. We also study the fidelity and Shannon entropy for such dynamics which, along with the presence of long-time finite imbalance, brings out the qualitatively different nature of QMBS in PXP ladders with $\Delta \sim 1$ from those in the PXP chain. Finally, we identify additional exact mid-spectrum zero modes that stay unchanged as a function of Δ and violate ETH.

Introduction:– ETH proposes that thermalization of local observables under purely unitary dynamics happens at the level of individual eigenstates of the Hamiltonian for many-body quantum systems [1–5]. Evasion of ETH can occur due to many-body localization (MBL) [6–14] in interacting systems with strong disorder. Such systems exhibit anomalous temporal relaxation of imbalance to a nonzero value starting from inhomogeneous initial states. This feature is often treated as an experimental signature of MBL [15, 16].

Recent quench experiments with a kinematically-constrained chain of 51 Rydberg atoms [17] showed non-trivial persistent revivals when initialized in a Néel state while other high-energy initial states showed rapid thermalization. This unusual behavior was shown, using a so-called PXP model [18–22], to be due to the substantial overlap of the Néel state with certain highly athermal ETH-violating states, dubbed QMBS, embedded in an otherwise ETH-satisfying spectrum [18, 19]. Other models with kinematic constraints in one and higher dimensions have already given several realizations for QMBS [23–38] (including in driven quantum matter [39–44]) as well as other anomalous dynamical features such as Hilbert space fragmentation [30, 45–49] and superdiffusive energy transport [50].

QMBS, in the PXP model, can be described within a forward scattering approximation (FSA) [18, 19] in terms of an *emergent* free spin whose magnitude scales linearly with system size [51–54]. Within FSA, the maximally up and down states of this “giant” spin are given by the period-2 Néel state and its translated partner. The persistent many-body revivals can then be interpreted as a coherent spin precession connecting these maximally up and down states [18, 19]. However, unlike in MBL, no long-time average imbalance survives dynamically for a quench from the inhomogeneous Néel state.

In this Letter, we consider a two-leg Rydberg ladder in the presence of finite Δ [55] which show several

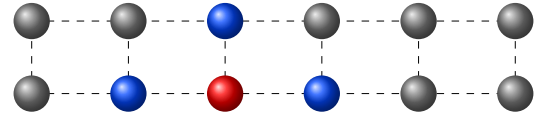


FIG. 1. A depiction of the Hilbert space constraint for the Hamiltonian in Eq. (1) for $N = 12$. A site with a Rydberg excited atom (red circle) implies that its nearest-neighbor sites (blue circles) cannot have another Rydberg excitation.

features of QMBS that are absent in the paradigmatic PXP chain. Mapping the presence (absence) of a Rydberg excitation to a $S = 1/2$ degree of freedom, $\sigma^z = +1$ (-1), we show that a quench from either the Néel or the vacuum state leads to site-dependent magnetization dynamics and to nonzero long-time average values for appropriately defined imbalance operators for $\Delta \gtrsim 0.5$ on finite-sized ladders. In contrast, these imbalances vanish for unitary dynamics from a generic initial state as per ETH. These constitute imbalance as a signature of scar-induced ETH violation; to our knowledge, such an effect has not been reported earlier in disorder-free systems. The PXP ladder studied here leads to persistent many-body revivals from both the Néel and the vacuum states (only Néel states) around $\Delta = 1$ ($\Delta = 0$). The analysis of the fidelity and Shannon entropy dynamics starting from these initial states indicates absence of a FSA picture in an unentangled Fock basis for QMBS in ladders around $\Delta \sim 1$; this feature, along with the presence of ETH violating imbalance as well as other anomalous mid-spectrum zero modes that stay unchanged [37, 56] as a function of Δ , sets these QMBS apart from their counterparts in PXP chains.

Model Hamiltonian:– We consider N $S = 1/2$ spins on the sites of a two-leg ladder, with L sites on each leg ($N = 2L$), described by the Hamiltonian:

$$\hat{\mathcal{H}} = -\Delta \sum_{j=1}^L \sum_{a=1}^2 (-1)^j \hat{\sigma}_{j,a}^z - w \sum_{j=1}^L \sum_{a=1}^2 \hat{\sigma}_{j,a}^x, \quad (1)$$

where $\Delta > 0$ denotes a staggered detuning while $w > 0$ is the coupling strength between the ground and excited states of Rydberg atoms. The site index (j, a) denotes the bottom [top] of the j -th rung with $(j, 1)$ [$(j, 2)$] (Fig. 1), $\hat{\sigma}_{j,a}^x := \hat{P}_{j,\bar{a}}^\downarrow \hat{P}_{j-1,a}^\downarrow \hat{P}_{j+1,a}^\downarrow \hat{\sigma}_{j,a}^x$ where (j, \bar{a}) denotes the other site that belongs to the same rung as (j, a) , with $\hat{P}_{j,a}^\downarrow = (1 - \hat{\sigma}_{j,a}^z)/2$. The string of \hat{P}^\downarrow operators ensures that no two nearest neighbor spins are simultaneously in the $\sigma^z = +1$ state for this ladder geometry (Fig. 1). We take periodic (open) boundary conditions along each leg (rung) of the ladder with even L , fix $w = \hbar = 1$ and $\Delta \in [0, 1]$ to stay well away from the integrable $\Delta \gg 1$ limit, and measure t in units of $\hbar w^{-1}$. The dimension of this constrained Hilbert space scales as $\mathcal{D}_H = (1 + \sqrt{2})^L + (1 - \sqrt{2})^L + (-1)^L$ [57].

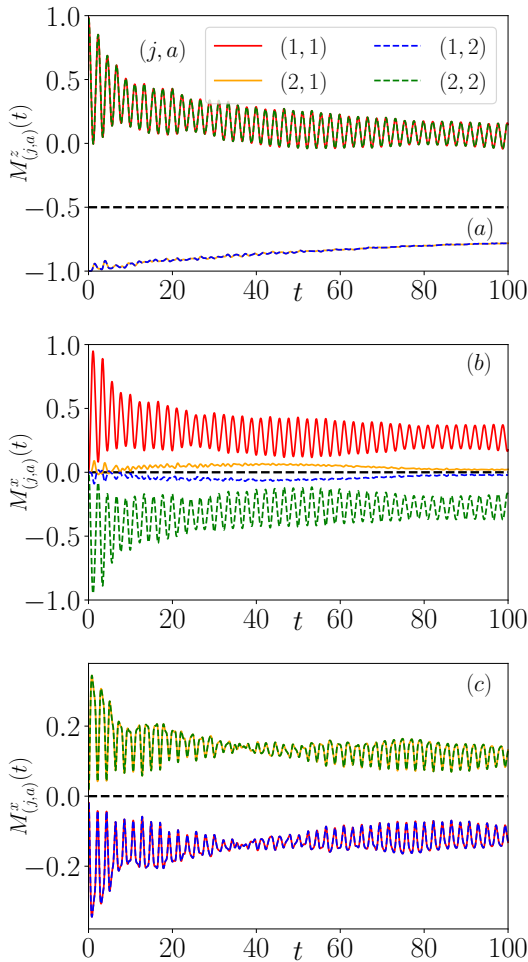


FIG. 2. Time evolution of (a) $M_{j,a}^z(t)$ and (b) $M_{j,a}^x(t)$ starting from $|\mathbb{Z}_2\rangle$ state for $j = 1, 2$ and $a = 1, 2$. (c) Plot of $M_{j,a}^x(t)$ starting from the $|\text{vac}\rangle$ state. For all plots, the color scheme follows panel (a), $w = 1 = \Delta$ and t is measured in units of $\hbar w^{-1}$.

Local magnetization dynamics: Similar to the PXP chain with a staggered field [19, 58], for every eigenstate $|E\rangle$ of $\hat{\mathcal{H}}$ (Eq. (1)) with eigenvalue E , there exists a chiral partner $|-E\rangle$ for any Δ . The $E \rightarrow -E$

symmetry of the spectrum fixes $\langle\langle \hat{\mathcal{H}} \rangle\rangle_{\beta=0} = 0$ ($\langle\langle \hat{\mathcal{H}} \rangle\rangle_{\beta}$ denotes a thermal average at inverse temperature β); thus typical initial states have a zero average energy density. Performing a quantum quench from an initial state $|\psi(0)\rangle$ such that $\langle\psi(0)|\hat{\mathcal{H}}|\psi(0)\rangle = 0$ implies that $\langle\psi(t)|\hat{\mathcal{A}}|\psi(t)\rangle = \langle\langle \hat{\mathcal{A}} \rangle\rangle_{\beta=0}$ for any local operator $\hat{\mathcal{A}}$ at late time from ETH if $N = 2L \gg 1$.

We probe the ergodicity of the model (Eq. (1)) by studying quench dynamics from the Néel $|\mathbb{Z}_2\rangle = |\bullet\circ\bullet\circ\bullet\rangle$ and vacuum $|\text{vac}\rangle = |\circ\circ\circ\circ\rangle$ states at $\Delta = 1$; these product states satisfy $\langle\psi(0)|\hat{\mathcal{H}}|\psi(0)\rangle = 0$ for any Δ . Here, the filled (open) circles denote $\sigma^z = +1(-1)$ on the corresponding sites (see Ref. [57] for dynamics from some other initial states with $\langle\psi(0)|\hat{\mathcal{H}}|\psi(0)\rangle = 0$).

In Fig. 2, we show the quench dynamics of such states for $N = 2L = 32$ by computing the dynamics of the site-resolved magnetization

$$M_{j,a}^{z[x]}(t) = \langle\psi(t)|\hat{\sigma}_{j,a}^z[\hat{\sigma}_{j,a}^{x}]|\psi(t)\rangle \quad (2)$$

starting from $|\mathbb{Z}_2\rangle$ and $|\text{vac}\rangle$ initial states at $\Delta = 1$ by evolving $|\psi(0)\rangle$ by integrating the Schrödinger equation as an initial value problem using the fourth-order Runge-Kutta integration scheme for $t \in [0, 100]$. For both initial states, we find $M_{j,a}^{z[x]} = M_{j\pm 2,a}^{z[x]}$; this ensures that Fig. 2, plotted for $j = 1, 2$ represents dynamics for any site j .

Starting the dynamics from $|\mathbb{Z}_2\rangle$ results in all spins that were initially $\sigma^z = +1$ (e.g., $M_{1,1}^z(t)$ and $M_{2,2}^z(t)$) oscillating around a superthermal value (i.e., higher than $\langle\langle \hat{\sigma}_{j,a}^z \rangle\rangle_{\beta=0}$). In contrast, the spins that were initially $\sigma^z = -1$ (e.g., $M_{1,2}^z(t)$ and $M_{2,1}^z(t)$) seem to approach a subthermal value without any oscillations (Fig. 2(a)). In general, we find $M_{2j-1,1}^z(t) = M_{2j,2}^z(t) \neq M_{2j,1}^z(t) = M_{2j-1,2}^z(t)$; this generates a longitudinal imbalance at $\Delta = 1$ for $t \in [0, 100]$. The corresponding $M_{j,a}^x(t)$ (Fig. 2(b)) for the sites that show oscillating longitudinal magnetization is sizeable in magnitude compared to the rest of the spins (for which it is close to 0 for these t): $M_{2j-1,1}^x(t) = -M_{2j,2}^x(t)$ and $M_{2j,1}^x(t) = -M_{2j-1,2}^x(t)$ with $|M_{2j,2}^x(t)| \ll |M_{2j,1}^x(t)|$. This generates a transverse imbalance.

In contrast, starting the dynamics from the vacuum state, one finds oscillating transverse magnetization (Fig. 2(c)) which satisfies $M_{2j-1,1}^x(t) = M_{2j-1,2}^x(t) = -M_{2j,1}^x(t) = -M_{2j,2}^x(t)$ for $t \in [0, 100]$ at $\Delta = 1$. This generates an imbalance in the transverse magnetization with half of the spins being superthermal (subthermal) for $t \in [0, 100]$. Some of these features can be analytically, albeit qualitatively, understood using a trial wavefunction [57].

These results indicate the following key differences of the local magnetization dynamics at $\Delta = 1$ from their counterparts in a PXP chain or a ladder at $\Delta = 0$. First, we find ETH violating local magnetization oscillations starting from the $|\text{vac}\rangle$ state which has no analogue in the latter systems. Second, the plots in Fig. 2 indicate a clear presence of imbalance for $t \gg 1$. We note that whereas the imbalance for short time dynamics may be expected due to the staggered detuning, its persistence at long times, away from the

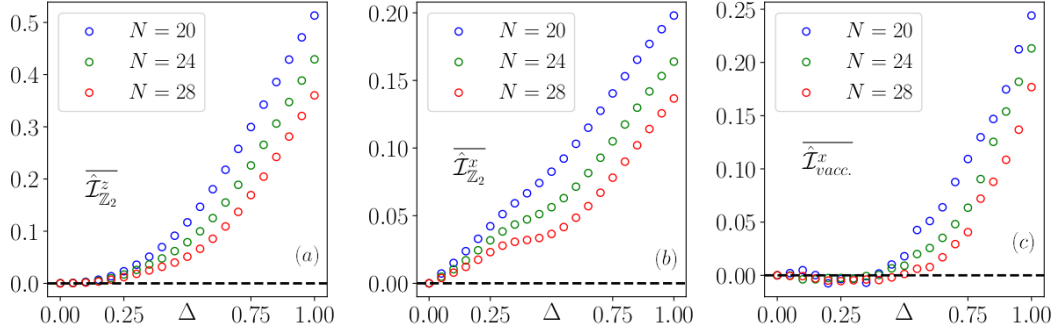


FIG. 3. Infinite time average value of local imbalances (a) $\hat{\mathcal{I}}_{\mathbb{Z}_2}^z$, (b) $\hat{\mathcal{I}}_{\mathbb{Z}_2}^x$ and (c) $\hat{\mathcal{I}}_{\text{vac}}^x$, for increasing values of Δ for $N = 20, 24, 28$.

integrable limit $\Delta \gg 1$, constitutes a clear indication of scar-induced imbalance in systems without disorder and provides a novel signature of weak ETH violation. Such an imbalance does not occur at $\Delta \simeq 0$ where the scar-induced oscillations lead to zero average imbalance. Moreover, such imbalance is present around $\Delta = 0.5$, at least from the Néel state, even though no persistent scar-induced oscillations occur around $\Delta = 0.5$ [57].

Behavior of Imbalance:- To further probe the nature of the imbalance, we define local imbalance operators for both longitudinal and transverse magnetizations as

$$\begin{aligned}\hat{\mathcal{I}}_{\mathbb{Z}_2}^z &= \frac{1}{L} \sum_{j=1}^L \sum_{a=1}^2 (s_1)_{ja} \hat{\sigma}_{j,a}^z, \quad \hat{\mathcal{I}}_{\mathbb{Z}_2}^x = \frac{1}{L} \sum_{j=1}^L \sum_{a=1}^2 (s_2)_{ja} \hat{\sigma}_{j,a}^x, \\ \hat{\mathcal{I}}_{\text{vac}}^x &= \frac{1}{L} \sum_{j=1}^L \sum_{a=1}^2 (s_3)_{ja} \hat{\sigma}_{j,a}^x.\end{aligned}\quad (3)$$

Here $(s_1) = (\uparrow\uparrow\uparrow\uparrow\cdots)$, $(s_2) = (\uparrow\uparrow\uparrow\uparrow\cdots)$ and $(s_3) = (\uparrow\uparrow\uparrow\uparrow\cdots)$ refer to particular sign structures assumed for the sites of the two-leg ladder [57]. Quenching the system from either $|\text{vac}\rangle$ or $|\mathbb{Z}_2\rangle$ leaves an imprint in long-time average values of these imbalance operators.

From ETH, it follows that the long-time average value of any local operator obeys

$$\overline{\hat{\mathcal{A}}} = \lim_{T \rightarrow \infty} \frac{1}{T} \int_0^T \langle \psi(t) | \hat{\mathcal{A}} | \psi(t) \rangle dt = \langle \hat{\mathcal{A}} \rangle_{\beta}, \quad (4)$$

where β is set by the average energy density of the initial state. For $|\mathbb{Z}_2\rangle$ and $|\text{vac}\rangle$ initial states $|\psi(0)\rangle$, $\beta = 0$ as discussed before. For such initial states, $\langle \hat{\mathcal{I}}_{\mathbb{Z}_2}^{x/z} \rangle_{\beta=0} = \langle \hat{\mathcal{I}}_{\text{vac}}^x \rangle_{\beta=0} = 0$ since $\langle \hat{\sigma}_{j,a}^z \rangle_{\beta=0}$ is independent of (j, a) and $\langle \hat{\sigma}_{j,a}^x \rangle_{\beta=0} = 0$. Thus, these imbalances should relax to zero from ETH for such initial states.

However, we find that quenching from either $|\text{vac}\rangle$ or $|\mathbb{Z}_2\rangle$ initial states leaves nonzero long-time average imbalances in finite-sized ladders which reflects a hitherto unexplored, signature of QMBS from specific initial states. To understand this, we express $\overline{\hat{\mathcal{A}}}$

(Eq. 4) using the ‘‘diagonal ensemble’’ [3]

$$\begin{aligned}\overline{\hat{\mathcal{A}}} &= \sum_{\mu \notin \mathcal{H}_0} |\langle \psi(0) | E_{\mu} \rangle|^2 (\hat{\mathcal{A}})_{\mu\mu} \\ &+ \sum_{\mu \in \mathcal{H}_0} |\langle \psi(0) | E_{\mu}^A \rangle|^2 (\hat{\mathcal{A}})_{\mu\mu}.\end{aligned}\quad (5)$$

In Eq. (5), the notation $\mu \in \mathcal{H}_0$ ($\mu \notin \mathcal{H}_0$) refer to the eigenstates of $\hat{\mathcal{H}}$ with $E = 0$ ($E \neq 0$). Furthermore, $|E_{\mu}^A\rangle$ refers to the basis of zero modes that diagonalizes $\hat{\mathcal{A}}$ in the zero mode subspace [58]. We note here that while an interacting non-integrable model such as the one considered here is expected to have a non-degenerate spectrum (apart from degeneracies induced by global symmetries), the PXP ladder contains an exponentially large number (in system size) of exact mid-spectrum zero modes ($E = 0$) that are protected by an index theorem [19, 56, 58] for any Δ [57].

We compute the long-time averages of the three imbalances using Eq. 5 for finite ladders upto $N = 28$ for various $\Delta \in [0, 1]$ using exact diagonalization (ED) and the results are displayed in Fig. 3. We find that $\overline{\hat{\mathcal{I}}_{\mathbb{Z}_2}^z}$, $\overline{\hat{\mathcal{I}}_{\mathbb{Z}_2}^x}$ and $\overline{\hat{\mathcal{I}}_{\text{vac}}^x}$, where the first two (last) imbalances (imbalance) are (is) calculated from the $|\mathbb{Z}_2\rangle$ ($|\text{vac}\rangle$) initial state, are all nonzero only when $\Delta \neq 0$. While $\overline{\hat{\mathcal{I}}_{\mathbb{Z}_2}^z}$ is monotonic as a function of Δ for a fixed N (Fig. 3(a)), $\overline{\hat{\mathcal{I}}_{\mathbb{Z}_2}^x}$ shows a nonmonotonic behavior around $\Delta \approx 0.5$ that sharpens with increasing N (Fig. 3(b)). The imbalance generated from the homogeneous vacuum state is even more nontrivial. The behavior of $\overline{\hat{\mathcal{I}}_{\text{vac}}^x}$ (Fig. 3(c)) shows that it becomes sizeable only when $\Delta \gtrsim 0.5$.

Explicit ED computations of Eq. (5) for both imbalances starting from the Néel state as well as analytic arguments [57] shows that nonzero contribution solely comes from the zero mode subspace. This clarifies how imbalance can be present around $\Delta = 0.5$ even though scar-induced oscillations are absent. Since both imbalances have a thermal expectation value of 0 for $\beta = 0$, this implies that $\sum_{\mu \in \mathcal{H}_0} \hat{\mathcal{A}}_{\mu\mu} = 0$ for both from ETH. To have $O(1)$ imbalances, $|\langle \psi(0) | E_{\mu}^A \rangle|^2$ in Eq. (5) should deviate strongly from a flat function in μ to one which gets sharply peaked when $\hat{\mathcal{A}}_{\mu\mu} \sim O(1)$.

This immediately implies that the $O(1)$ values of the long-time average imbalances starting from the Néel state are due to “anomalous” zero modes that have a strong overlap with this initial state. These modes are anomalous because a typical zero mode, that mimics a featureless infinite-temperature state from ETH, will only have $O(1/\mathcal{D}_H)$ overlap with the Néel state. The long-time average of the transverse imbalance from the vacuum state receives contributions both from zero and nonzero modes. However, an $O(1)$ imbalance again implies QMBS that have a high overlap with the vacuum state.

The features of the magnetization dynamics and imbalance seen above may be tied to the presence of two chirality operators $\mathcal{C}_1 = T_x \mathcal{C}$ and $\mathcal{C}_2 = T_x T_y \mathcal{C}$, where $T_{x(y)}$ are translation operator along (perpendicular) to the chains and $\mathcal{C} = \prod_j \prod_{a=1,2} \sigma_{j,a}^z$, that satisfy $\{H, \mathcal{C}_{1,2}\} = 0$. Using their properties, it is possible to show that [57] for all $E \neq 0$ eigenstates $\langle E_\mu | \sigma_{j,a}^z | E_\nu \rangle = \langle -E_\mu | \sigma_{j+1,a}^z | -E_\nu \rangle = \langle -E_\mu | \sigma_{j+1,\bar{a}}^z | -E_\nu \rangle$; moreover, $|\langle \psi(0) | E_\mu \rangle| = |\langle \psi(0) | -E_\mu \rangle|$ for $|\psi(0)\rangle = |\mathbb{Z}_2\rangle$. Thus the difference in dynamics of $M_{1,1}^z(t)$ and $M_{1,2}^z(t)$ and hence $\mathcal{I}_{\mathbb{Z}_2}^z$ do not receive any contribution from the $E \neq 0$ states. Rather, it is entirely due to the contribution of states from the zero energy sector with which $|\mathbb{Z}_2\rangle$ has a large overlap. A similar analysis [57] shows $\langle E_\mu | \sigma_{j,a}^x | E_\nu \rangle = -\langle -E_\mu | \sigma_{j+1,\bar{a}}^x | -E_\nu \rangle$ for the transverse magnetization and leads to $M_{2j-1,1}^x(t) = -M_{2j,2}^x(t)$ and a net transverse imbalance. Finally, an identical analysis for the $|\text{vac}\rangle$ state yields $M_{j,a}^z(t) = M_{j+1,a}^z(t) = M_{j+1,\bar{a}}^z(t)$ leading to zero imbalance; in contrast, the transverse magnetization satisfies $M_{j,a}^x(t) = -M_{j+1,\bar{a}}^x(t)$ and shows a finite $\mathcal{I}_{\text{vac}}^x$.

Fidelity and Shannon entropy dynamics:– To understand the qualitatively different nature of the scar-induced oscillations around $\Delta = 1$ and $\Delta = 0$, it is instructive to monitor the time evolution of both fidelity $\mathcal{F}(t) = |\langle \psi(t) | \psi(0) \rangle|^2$ and Shannon entropy $S_1(t) = -\sum_{\alpha=1}^{\mathcal{D}_H} |\psi_\alpha(t)|^2 \log(|\psi_\alpha(t)|^2)$ where $|\psi(t)\rangle = \sum_{\alpha=1}^{\mathcal{D}_H} \psi_\alpha(t) |\alpha\rangle$ when $|\psi(t)\rangle$ is expressed in the classical Fock basis $|\alpha\rangle$ diagonal in σ^z . $S_1(t)$ directly probes the spread of $|\psi(t)\rangle$ in this Fock basis.

At $\Delta = 0$ [Fig. 4(a)] ($\Delta = 1$ [Fig. 4(b)]), there are pronounced periodic revivals in $\mathcal{F}(t)$ when the system is initialized in the $|\mathbb{Z}_2\rangle$ state unlike the rapid decay to zero expected from ETH. However, the behavior of $S_1(t)$ shows a striking difference between $\Delta = 0$ and $\Delta = 1$. While $S_1(t)$ shows local minima at the same $(t^*, 2t^*, 3t^*, \dots)$ as the revivals in $\mathcal{F}(t)$ in both cases, it shows additional pronounced local minima at $(t^*/2, 3t^*/2, 5t^*/2, \dots)$ for $\Delta = 0$ which are absent for $\Delta = 1$. Such additional local minima in $S_1(t)$ are also present starting from both period-2 and period-3 initial states for the PXP chain [57].

These additional minima in $S_1(t)$ at $\Delta = 0$ are due to local maxima in $|\langle \bar{\mathbb{Z}}_2 | \exp(-i\hat{H}t) | \mathbb{Z}_2 \rangle|^2$ at $(t^*/2, 3t^*/2, 5t^*/2, \dots)$ where the state $|\psi(t)\rangle$ can again be approximated by $|\bar{\mathbb{Z}}_2\rangle$ which is related to $|\mathbb{Z}_2\rangle$ by $\sigma^z \rightarrow -\sigma^z$ on all sites. Thus, the persistent many-body revivals can be interpreted as a coherent spin precession of an emergent giant spin whose maximally po-

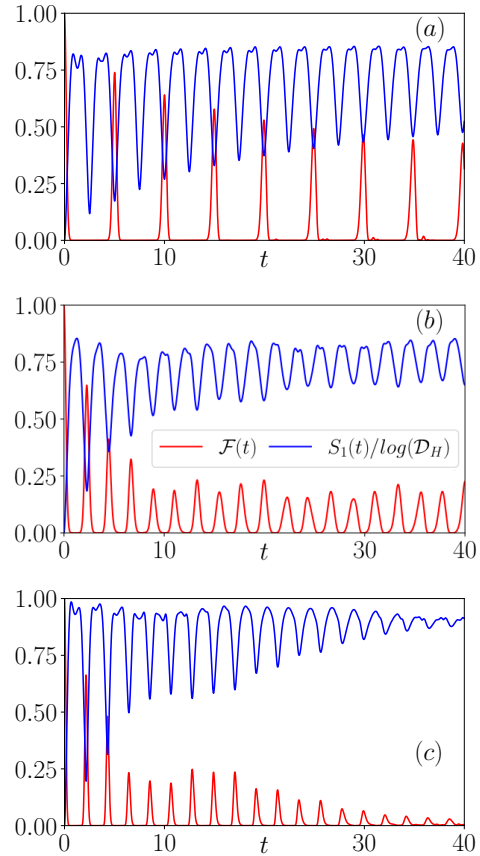


FIG. 4. Evolution of fidelity $\mathcal{F}(t)$ (in red) and (normalized) Shannon entropy $S_1/\log(\mathcal{D}_H)$ (in blue) of $N = 32$ ladder for (a) $\Delta = 0$, $|\psi(0)\rangle = |\mathbb{Z}_2\rangle$, (b) $\Delta = 1$, $|\psi(0)\rangle = |\mathbb{Z}_2\rangle$ and (c) $\Delta = 1$, $|\psi(0)\rangle = |\text{vac}\rangle$.

larized states may be approximated by $|\mathbb{Z}_2\rangle$ and $|\bar{\mathbb{Z}}_2\rangle$ respectively. This PXP-like scarring regime from $|\mathbb{Z}_2\rangle$ persists from $\Delta = 0$ upto $\Delta \approx 0.2$ from the $N = 32$ data [57]. Interestingly, the timescale of fidelity revivals is remarkably close to that obtained from two independent PXP chains, where both chains are individually initialized to Néel states, with one being a translated partner of the other to maintain the Hilbert space constraints on a ladder.

On the other hand, the many-body revivals from $|\mathbb{Z}_2\rangle$ for $\Delta = 1$ cannot be interpreted in terms of two end states where the other either appears classical or can be approximated by a superposition of a small number of Fock states. This non-PXP-like scarring regime from $|\mathbb{Z}_2\rangle$ persists from $\Delta \approx 0.75$ onward from the $N = 32$ data [57]. The many-body revivals in $\mathcal{F}(t)$ starting from the $|\text{vac}\rangle$ state at $\Delta = 1$ (Fig. 4 (c)) behaves similarly with the local minima of $S_1(t)$ coinciding with the maxima of $\mathcal{F}(t)$. The revivals from the $|\text{vac}\rangle$ state does not have any analog in the PXP chain and this non-PXP-like scarring regime from $|\text{vac}\rangle$ persists from $\Delta \approx 0.7$ onward from the $N = 32$ data [57]. The corresponding entanglement entropy dynamics [57] in both cases suggests that the other end state may have a more natural description in a basis

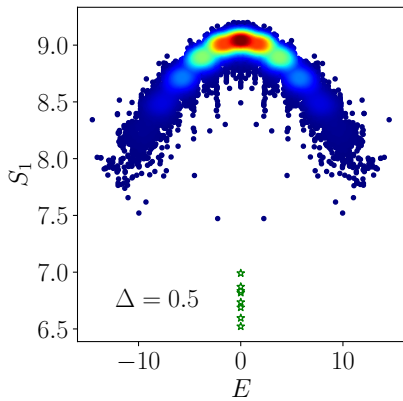


FIG. 5. Shannon entropy S_1 of all eigenvectors (where warm colors indicate a higher density of states in the colormap) versus the anomalous zero modes (green star points) that stay unchanged as a function of Δ for $N = 24$ and $\Delta = 0.5$.

where entanglement of spin pairs on an extensive number of individual rungs plays a crucial role, leading to a breakdown of the *independent* chain picture.

In all cases with such periodic revivals, monitoring $|\langle \mathbb{Z}_2 | E \rangle|^2$ and $|\langle \text{vac} | E \rangle|^2$ from ED data shows towers of states with anomalously high overlap with these initial states which are approximately equidistant in energy with a spacing of δE near the middle of the spectrum. The revival timescale of $\mathcal{F}(t)$ are related to δE by $t^* \approx 2\pi/\delta E$ [57]. However, the timescale for oscillations in local magnetization is $t^*/2$ (t^* from the initial $|\mathbb{Z}_2\rangle$ state in the PXP-scarring (non-PXP scarring) regime (Fig. 2 and Ref. [57]).

Additional anomalous zero modes:—The spectrum of this model possesses other anomalous zero modes apart from the ones that contribute to the long-time average imbalances (Eq. 5). These are *simultaneous* zero modes of both the non-commuting terms in $\hat{\mathcal{H}}$ (Eq. 1), i.e., $\sum_{j=1}^L \sum_{a=1}^2 (-1)^j \hat{\sigma}_{j,a}^z$ and $\sum_{j=1}^L \sum_{a=1}^2 \hat{\sigma}_{j,a}^x$. Since such eigenstates stay unchanged as Δ is varied in spite of the exponentially small (in system size) energy level spacing in their neighborhood, these necessarily violate ETH [28]. While the existence of such anomalous zero modes can be shown even in the thermodynamic limit for certain interacting models [37, 56], here we demonstrate their presence using ED on finite-sized ladders. Since a typical zero mode is expected to satisfy ETH and coexists with such anomalous zero modes at the same energy, a further numerical procedure is required to identify them from ED [32]. This gives $\mathcal{N}_0 = 1, 3, 6, 8, 9, 8$ for ladders with $N = 4, 8, 12, 16, 20, 24$, where \mathcal{N}_0 is the number of such anomalous zero modes.

We show the data for the Shannon entropy S_1 for all eigenstates obtained for a ladder with $N = 24$ at $\Delta = 0.5$ from ED in Fig. 5. The Shannon entropy of the zero modes that stay unchanged with Δ has been shown as green star points in Fig. 5. It is clear that these modes are much more localized in the Hilbert space than any typical zero mode. To our knowledge,

simultaneous zero modes have not been demonstrated in the context of PXP chains.

Conclusions and outlook:— We have considered a kinematically-constrained model of Rydberg atoms on finite two-leg ladders in the presence of a staggered detuning and demonstrated several new features of QMBS in its spectrum that are absent in the paradigmatic PXP chain (or ladder at $\Delta = 0$). Most strikingly, quantum quenches from either the Néel or the vacuum state generate nonzero long-time imbalance averages for finite Δ . These imbalances can be probed dynamically by monitoring the site-resolved magnetizations; they decay to zero for dynamics from generic initial states for which ETH is obeyed. We have also demonstrated the co-existence of QMBS that have large overlaps with both the Néel and the vacuum initial states, something which has no analog in PXP chains. Anomalous mid-spectrum zero modes that stay unchanged as a function of the staggered detuning strength have also been shown.

Several open questions arise from our study. While the imbalance operators certainly acquire a nonzero long-time average value, these do not necessarily converge to a time-independent value at late times, unlike the case of MBL; this issue deserves further study. Also, while a PXP-like scarring regime exists for these ladders at small enough Δ , it seems that the regime of co-existing QMBS with large overlap with both Néel and vacuum states might not have any simple FSA description in an unentangled basis and may require a basis with an extensive number of locally entangled units. A better understanding using ideas similar to the ones explained in Refs. 53 and 54 is left as a subject of future study. Lastly, understanding the nature of the simultaneous zero modes that stay unchanged with the staggered detuning and possibly showing their existence in the thermodynamic limit are interesting open questions.

Acknowledgement: KS thanks DST for support through JCB/2021/000030. AS thanks Ajit C. Balaram and MP thanks Tista Banerjee for discussions. MS acknowledges the support from UK EPSRC award under the Agreement EP/Y005090/1.

-
- [1] J. M. Deutsch, Quantum statistical mechanics in a closed system, *Phys. Rev. A* **43**, 2046 (1991).
 - [2] M. Srednicki, Chaos and quantum thermalization, *Phys. Rev. E* **50**, 888 (1994).
 - [3] M. Rigol, V. Dunjko, and M. Olshanii, Thermalization and its mechanism for generic isolated quantum systems, *Nature* **452**, 854 (2008).
 - [4] L. D'Alessio, Y. Kafri, A. Polkovnikov, and M. Rigol, From quantum chaos and eigenstate thermalization to statistical mechanics and thermodynamics, *Advances in Physics* **65**, 239 (2016), <https://doi.org/10.1080/00018732.2016.1198134>.
 - [5] A. Dymarsky, N. Lashkari, and H. Liu, Subsystem eigenstate thermalization hypothesis, *Phys. Rev. E* **97**, 012140 (2018).
 - [6] D. Basko, I. Aleiner, and B. Altshuler, Metal-insulator

- transition in a weakly interacting many-electron system with localized single-particle states, *Annals of Physics* **321**, 1126 (2006).
- [7] D. M. Basko, I. L. Aleiner, and B. L. Altshuler, Possible experimental manifestations of the many-body localization, *Phys. Rev. B* **76**, 052203 (2007).
- [8] V. Oganesyan and D. A. Huse, Localization of interacting fermions at high temperature, *Phys. Rev. B* **75**, 155111 (2007).
- [9] A. Pal and D. A. Huse, Many-body localization phase transition, *Phys. Rev. B* **82**, 174411 (2010).
- [10] R. Nandkishore and D. A. Huse, Many-body localization and thermalization in quantum statistical mechanics, *Annual Review of Condensed Matter Physics* **6**, 15 (2015), <https://doi.org/10.1146/annurev-conmatphys-031214-014726>.
- [11] D. A. Abanin, E. Altman, I. Bloch, and M. Serbyn, Colloquium: Many-body localization, thermalization, and entanglement, *Rev. Mod. Phys.* **91**, 021001 (2019).
- [12] N. Macé, F. Alet, and N. Laflorencie, Multifractal scalings across the many-body localization transition, *Phys. Rev. Lett.* **123**, 180601 (2019).
- [13] M. Serbyn, Z. Papić, and D. A. Abanin, Local conservation laws and the structure of the many-body localized states, *Phys. Rev. Lett.* **111**, 127201 (2013).
- [14] D. A. Huse, R. Nandkishore, and V. Oganesyan, Phenomenology of fully many-body-localized systems, *Phys. Rev. B* **90**, 174202 (2014).
- [15] M. Schreiber, S. S. Hodgman, P. Bordia, H. P. Lüschen, M. H. Fischer, R. Vosk, E. Altman, U. Schneider, and I. Bloch, Observation of many-body localization of interacting fermions in a quasirandom optical lattice, *Science* **349**, 842 (2015), <https://www.science.org/doi/pdf/10.1126/science.aaa7432>.
- [16] J. Smith, A. Lee, P. Richerme, B. Neyenhuis, P. W. Hess, P. Hauke, M. Heyl, D. A. Huse, and C. Monroe, Many-body localization in a quantum simulator with programmable random disorder, *Nature Physics* **12**, 907 (2016).
- [17] H. Bernien, S. Schwartz, A. Keesling, H. Levine, A. Omran, H. Pichler, S. Choi, A. S. Zibrov, M. Endres, M. Greiner, V. Vuletić, and M. D. Lukin, Probing many-body dynamics on a 51-atom quantum simulator, *Nature* **551**, 579 (2017).
- [18] C. J. Turner, A. A. Michailidis, D. A. Abanin, M. Serbyn, and Z. Papić, Weak ergodicity breaking from quantum many-body scars, *Nature Physics* **14**, 745 (2018).
- [19] C. J. Turner, A. A. Michailidis, D. A. Abanin, M. Serbyn, and Z. Papić, Quantum scarred eigenstates in a rydberg atom chain: Entanglement, breakdown of thermalization, and stability to perturbations, *Phys. Rev. B* **98**, 155134 (2018).
- [20] S. Sachdev, K. Sengupta, and S. M. Girvin, Mott insulators in strong electric fields, *Phys. Rev. B* **66**, 075128 (2002).
- [21] P. Fendley, K. Sengupta, and S. Sachdev, Competing density-wave orders in a one-dimensional hard-boson model, *Phys. Rev. B* **69**, 075106 (2004).
- [22] I. Lesanovsky and H. Katsura, Interacting fibonacci anyons in a rydberg gas, *Phys. Rev. A* **86**, 041601 (2012).
- [23] C.-J. Lin and O. I. Motrunich, Exact quantum many-body scar states in the rydberg-blockaded atom chain, *Phys. Rev. Lett.* **122**, 173401 (2019).
- [24] S. Ok, K. Choo, C. Mudry, C. Castelnovo, C. Chamon, and T. Neupert, Topological many-body scar states in dimensions one, two, and three, *Phys. Rev. Res.* **1**, 033144 (2019).
- [25] T. Iadecola and M. Schechter, Quantum many-body scar states with emergent kinetic constraints and finite-entanglement revivals, *Phys. Rev. B* **101**, 024306 (2020).
- [26] C.-J. Lin, V. Calvera, and T. H. Hsieh, Quantum many-body scar states in two-dimensional rydberg atom arrays, *Phys. Rev. B* **101**, 220304 (2020).
- [27] F. M. Surace, M. Votto, E. G. Lazo, A. Silva, M. Dalmonte, and G. Giudici, Exact many-body scars and their stability in constrained quantum chains, *Phys. Rev. B* **103**, 104302 (2021).
- [28] D. Banerjee and A. Sen, Quantum scars from zero modes in an abelian lattice gauge theory on ladders, *Phys. Rev. Lett.* **126**, 220601 (2021).
- [29] V. Karle, M. Serbyn, and A. A. Michailidis, Area-law entangled eigenstates from nullspaces of local hamiltonians, *Phys. Rev. Lett.* **127**, 060602 (2021).
- [30] B. Mukherjee, Z. Cai, and W. V. Liu, Constraint-induced breaking and restoration of ergodicity in spin-1 pxp models, *Phys. Rev. Res.* **3**, 033201 (2021).
- [31] C. M. Langlett, Z.-C. Yang, J. Wildeboer, A. V. Gorshkov, T. Iadecola, and S. Xu, Rainbow scars: From area to volume law, *Phys. Rev. B* **105**, L060301 (2022).
- [32] S. Biswas, D. Banerjee, and A. Sen, Scars from protected zero modes and beyond in $U(1)$ quantum link and quantum dimer models, *SciPost Phys.* **12**, 148 (2022).
- [33] A. S. Aramthottil, U. Bhattacharya, D. González-Cuadra, M. Lewenstein, L. Barbiero, and J. Zakrzewski, Scar states in deconfined F_2 lattice gauge theories, *Phys. Rev. B* **106**, L041101 (2022).
- [34] S.-Y. Zhang, D. Yuan, T. Iadecola, S. Xu, and D.-L. Deng, Extracting quantum many-body scarred eigenstates with matrix product states, *Phys. Rev. Lett.* **131**, 020402 (2023).
- [35] J.-Y. Desaulles, D. Banerjee, A. Hudomal, Z. Papić, A. Sen, and J. C. Halimeh, Weak ergodicity breaking in the schwinger model, *Phys. Rev. B* **107**, L201105 (2023).
- [36] J.-Y. Desaulles, A. Hudomal, D. Banerjee, A. Sen, Z. Papić, and J. C. Halimeh, Prominent quantum many-body scars in a truncated schwinger model, *Phys. Rev. B* **107**, 205112 (2023).
- [37] I. Sau, P. Stornati, D. Banerjee, and A. Sen, Sublattice scars and beyond in two-dimensional $u(1)$ quantum link lattice gauge theories, *Phys. Rev. D* **109**, 034519 (2024).
- [38] T. Budde, M. K. Marinković, and J. C. P. Barros, Quantum many-body scars for arbitrary integer spin in 2+1d abelian gauge theories (2024), [arXiv:2403.08892 \[hep-lat\]](https://arxiv.org/abs/2403.08892).
- [39] K. Mizuta, K. Takasan, and N. Kawakami, Exact floquet quantum many-body scars under rydberg blockade, *Phys. Rev. Res.* **2**, 033284 (2020).
- [40] B. Mukherjee, S. Nandy, A. Sen, D. Sen, and K. Sengupta, Collapse and revival of quantum many-body scars via floquet engineering, *Phys. Rev. B* **101**, 245107 (2020).
- [41] B. Mukherjee, A. Sen, D. Sen, and K. Sengupta, Dynamics of the vacuum state in a periodically driven rydberg chain, *Phys. Rev. B* **102**, 075123 (2020).
- [42] B. Mukherjee, A. Sen, D. Sen, and K. Sengupta, Restoring coherence via aperiodic drives in a many-body quantum system, *Phys. Rev. B* **102**, 014301 (2020).
- [43] B. Mukherjee, A. Sen, and K. Sengupta, Periodically driven rydberg chains with staggered detuning, *Phys.*

- [Rev. B **106**, 064305 \(2022\)](#).
- [44] A. Hudomal, J.-Y. Desaulles, B. Mukherjee, G.-X. Su, J. C. Halimeh, and Z. Papić, Driving quantum many-body scars in the pxp model, [Phys. Rev. B **106**, 104302 \(2022\)](#).
 - [45] C. M. Langlett and S. Xu, Hilbert space fragmentation and exact scars of generalized fredkin spin chains, [Phys. Rev. B **103**, L220304 \(2021\)](#).
 - [46] B. Mukherjee, D. Banerjee, K. Sengupta, and A. Sen, Minimal model for hilbert space fragmentation with local constraints, [Phys. Rev. B **104**, 155117 \(2021\)](#).
 - [47] A. Chattopadhyay, B. Mukherjee, K. Sengupta, and A. Sen, Strong Hilbert space fragmentation via emergent quantum drums in two dimensions, [SciPost Phys. **14**, 146 \(2023\)](#).
 - [48] P. Brighi, M. Ljubotina, and M. Serbyn, Hilbert space fragmentation and slow dynamics in particle-conserving quantum East models, [SciPost Phys. **15**, 093 \(2023\)](#).
 - [49] M. Ganguli, S. Aditya, and D. Sen, [Aspects of Hilbert space fragmentation in the quantum East model: fragmentation, subspace-restricted quantum scars, and effects of density-density interactions \(2024\)](#), [arXiv:2409.15943 \[cond-mat.stat-mech\]](#).
 - [50] M. Ljubotina, J.-Y. Desaulles, M. Serbyn, and Z. Papić, Superdiffusive energy transport in kinetically constrained models, [Phys. Rev. X **13**, 011033 \(2023\)](#).
 - [51] W. W. Ho, S. Choi, H. Pichler, and M. D. Lukin, Periodic orbits, entanglement, and quantum many-body scars in constrained models: Matrix product state approach, [Phys. Rev. Lett. **122**, 040603 \(2019\)](#).
 - [52] C. J. Turner, J.-Y. Desaulles, K. Bull, and Z. Papić, Correspondence principle for many-body scars in ultracold rydberg atoms, [Phys. Rev. X **11**, 021021 \(2021\)](#).
 - [53] K. Omiya and M. Müller, Quantum many-body scars in bipartite rydberg arrays originating from hidden projector embedding, [Phys. Rev. A **107**, 023318 \(2023\)](#).
 - [54] K. Omiya and M. Müller, Fractionalization paves the way to local projector embeddings of quantum many-body scars, [Phys. Rev. B **108**, 054412 \(2023\)](#).
 - [55] M. Sarkar, M. Pal, A. Sen, and K. Sengupta, Quantum order-by-disorder induced phase transition in Rydberg ladders with staggered detuning, [SciPost Phys. **14**, 004 \(2023\)](#).
 - [56] A. Udupa, S. Sur, S. Nandy, A. Sen, and D. Sen, Weak universality, quantum many-body scars, and anomalous infinite-temperature autocorrelations in a one-dimensional spin model with duality, [Phys. Rev. B **108**, 214430 \(2023\)](#).
 - [57] See Supplemental Material for further details.
 - [58] M. Schechter and T. Iadecola, Many-body spectral reflection symmetry and protected infinite-temperature degeneracy, [Phys. Rev. B **98**, 035139 \(2018\)](#).

Supplementary Information

CONTENTS

S1. Hilbert Space Dimension	1
S2. Magnetization Dynamics from $ \mathbb{Z}_2\rangle, \mathbb{Z}_3\rangle, \mathbb{Z}_4\rangle$ and $ \text{vac}\rangle$ initial states	2
S3. Single plaquette wavefunction	2
S4. Chirality operators and spectral reflection symmetry	6
S5. Derivation of some exact aspects	7
A. Long-time average values of imbalance operators $\hat{I}_{ \mathbb{Z}_2\rangle}^z$ and $\hat{I}_{ \mathbb{Z}_2\rangle}^x$	7
B. Instantaneous site-resolved magnetizations $\langle \hat{\sigma}_{i,a}^z \rangle_t$ and $\langle \hat{\sigma}_{i,a}^x \rangle_t$	9
S6. Fidelity and Shannon entropy dynamics from $ \mathbb{Z}_2\rangle$ and $ \mathbb{Z}_3\rangle$ initial states in PXP chains	11
S7. PXP and non-PXP regimes of many-body revivals in ladders	12
S8. Overlap of many-body eigenstates with $ \mathbb{Z}_2\rangle$ and $ \text{vac}\rangle$	13

S1. HILBERT SPACE DIMENSION

At inverse temperature β , the partition function of a quantum theory with Hamiltonian $\hat{\mathcal{H}}$ reads $\mathcal{Z}(\beta) = \text{Tr}(e^{-\beta\hat{\mathcal{H}}})$ which implies $\mathcal{Z}(\beta \rightarrow 0) = \text{Tr}(1) = \mathcal{D}_H$. The quantity $\mathcal{Z}(\beta \rightarrow 0)$ for Eq. (1) of main text can be found from the eigenvalues of the corresponding transfer matrix T , since $\mathcal{Z}(\beta \rightarrow 0) = \text{Tr}(T^L)$. We note that the state $|\bullet\rangle$ is prohibited due to Rydberg blockade. Using this, in the basis $\{|\bullet\rangle, |\circ\rangle, |\circ\rangle\}$, the transfer matrix T can be written as

$$T = \begin{pmatrix} 0 & 1 & 1 \\ 1 & 0 & 1 \\ 1 & 1 & 1 \end{pmatrix}. \quad (\text{S1})$$

The eigenvalues of the matrix T are $\lambda = -1, 1 \pm \sqrt{2}$ which implies $\mathcal{D}_H = (1 + \sqrt{2})^L + (1 - \sqrt{2})^L + (-1)^L$ as given in the main text. Furthermore, since both the product states $|\mathbb{Z}_2\rangle = |\bullet\circ\bullet\circ\bullet\circ\rangle$ and $|\text{vac}\rangle = |\circ\circ\circ\circ\rangle$ lie in the sector with $k_x = 0$ (with respect to translations $(j, a) \rightarrow (j + 2, a)$ which is also a symmetry of the Hamiltonian), we give the relevant Hilbert space dimension for $k_x = 0$ below.

$N (= 2L)$	$\mathcal{D}_H, \text{ full}$	$\mathcal{D}_H, k_x = 0$
4	7	7
8	35	21
12	199	71
16	1155	301
20	6727	1351
24	39203	6581
28	228487	32647
32	1331715	166621

TABLE I. Hilbert space dimensions of the model (Eq. (1) of main text) for various system sizes and $k_x = 0$ translational symmetry sector.

S2. MAGNETIZATION DYNAMICS FROM $|\mathbb{Z}_2\rangle, |\mathbb{Z}_3\rangle, |\mathbb{Z}_4\rangle$ AND $|\text{vac}\rangle$ INITIAL STATES

We probe the ergodicity of the model by studying quench dynamics from the following particular product states $|\mathbb{Z}_2\rangle = |\bullet\circ\bullet\circ\bullet\circ\cdots\rangle$, $|\mathbb{Z}_3\rangle = |\bullet\circ\circ\bullet\circ\circ\cdots\rangle$, $|\mathbb{Z}_4\rangle = |\circ\circ\circ\bullet\circ\circ\cdots\rangle$, $|\text{vac}\rangle = |\circ\circ\circ\circ\circ\cdots\rangle$, all of which satisfy $\langle\psi(0)|\hat{\mathcal{H}}|\psi(0)\rangle = 0$ for any Δ . Here, the filled (open) circles denote $\sigma^z = +1(-1)$ on the corresponding sites and $|\mathbb{Z}_2\rangle$ ($|\text{vac}\rangle$) denotes a Rydberg Néel (vacuum) state. While $|\mathbb{Z}_2\rangle$ and $|\text{vac}\rangle$ are compatible with any even L , $|\mathbb{Z}_3\rangle$ ($|\mathbb{Z}_4\rangle$) needs L to be a multiple of 3 (4). In Fig. S1, we show the quench dynamics of such states for $N = 2L = 24$ for three different values of Δ and observe the time evolution of $\hat{M}_z = \frac{1}{N} \sum_{j=1}^L \sum_{a=1}^2 \hat{\sigma}_{j,a}^z$ (longitudinal magnetization density).

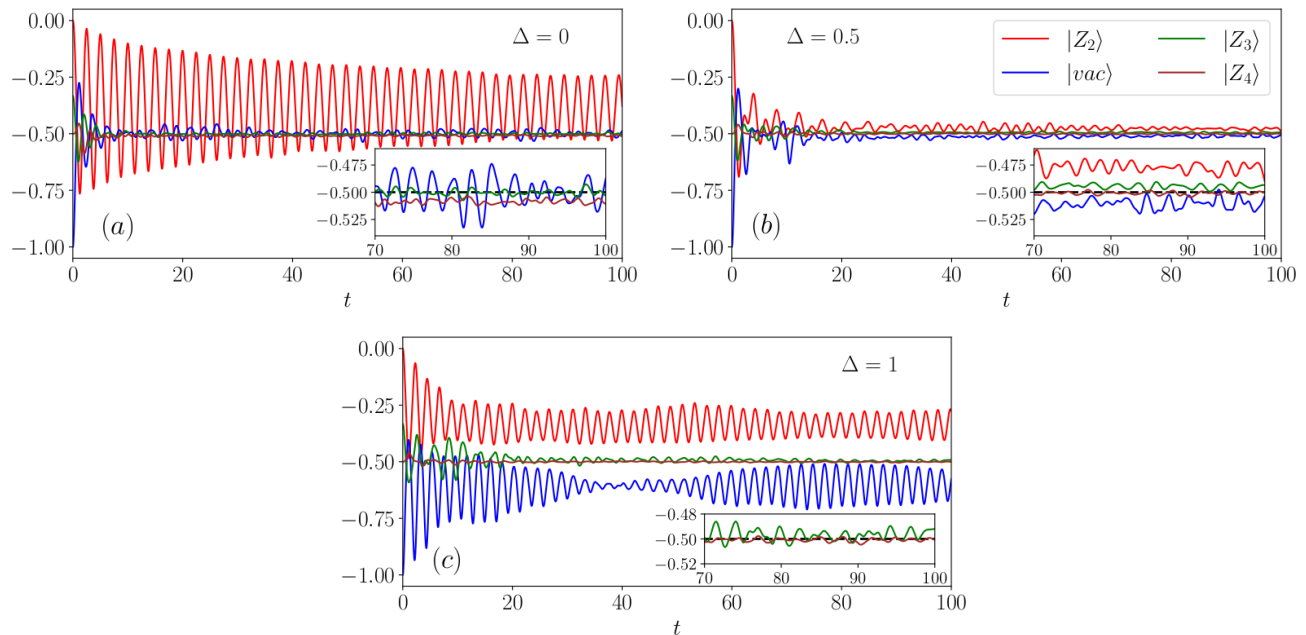


FIG. S1. Time evolution of longitudinal magnetization density $\langle\psi(t)|\hat{M}_z|\psi(t)\rangle$ starting from simple initial states $|\mathbb{Z}_2\rangle$ (red), $|\text{vac}\rangle$ (blue), $|\mathbb{Z}_3\rangle$ (green) and $|\mathbb{Z}_4\rangle$ (brown) for (a) $\Delta = 0$, (b) $\Delta = 0.5$ and (c) $\Delta = 1$ for a $N = 24$ ladder. The insets display the late time behaviour more clearly; the horizontal dotted line in black indicates $\langle\hat{M}_z\rangle_{\beta=0}$.

In all cases ($\Delta = 0.0, 0.5, 1.0$) displayed in Fig. S1, we see that starting from $|\mathbb{Z}_3\rangle$ and $|\mathbb{Z}_4\rangle$ initial states, the local operator \hat{M}_z relaxes close to $\langle\hat{M}_z\rangle_{\beta=0}$ (see insets of the panels, where $\langle\hat{M}_z\rangle_{\beta=0}$ is denoted by a dotted horizontal black line for clarity) for $t \gg 1$ as can be expected from ETH. For $\Delta = 0$ (Fig. S1 (a)), even the $|\text{vac}\rangle$ state seems to relax locally to $\beta = 0$, while there are clear oscillations from the $|\mathbb{Z}_2\rangle$ state reminiscent of the PXP chain. Increasing Δ to 0.5 (Fig. S1 (b)) leads to all 4 initial states relaxing locally to $\beta = 0$. Remarkably, the oscillations from $|\mathbb{Z}_2\rangle$ reappear as Δ is increased further to 1 (Fig. S1 (c)). In fact, even the $|\text{vac}\rangle$ state leads to oscillations in the longitudinal magnetization density at $\Delta = 1$ (Fig. S1 (c)) which has no analog in the PXP chain.

S3. SINGLE PLAQUETTE WAVEFUNCTION

In this section, we construct exact eigenstates of a single plaquette of the ladder and use them to obtain analytic understanding of certain properties of the imbalance. To this end, we chart out the Fock states for a single plaquette of the ladder

$$|\mathcal{F}_0\rangle = |\circ\circ\rangle, \quad |\mathcal{F}_1\rangle = |\bullet\circ\rangle, \quad |\mathcal{F}_2\rangle = |\circ\bullet\rangle, \quad |\mathcal{F}_3\rangle = |\bullet\bullet\rangle, \quad |\mathcal{F}_4\rangle = |\circ\circ\rangle, \quad |\mathcal{F}_5\rangle = |\bullet\bullet\rangle, \quad |\mathcal{F}_6\rangle = |\circ\bullet\rangle \quad (\text{S2})$$

The Hamiltonian matrix, in the basis of these Fock states, can be written in terms of a single dimensionless parameter $r = w/(2\Delta)$ as

$$H = \begin{pmatrix} 0 & r & r & r & r & 0 & 0 \\ r & -1 & 0 & 0 & 0 & r & 0 \\ r & 0 & 1 & 0 & 0 & 0 & r \\ r & 0 & 0 & -1 & 0 & 0 & r \\ r & 0 & 0 & 0 & 1 & r & 0 \\ 0 & r & 0 & 0 & r & 0 & 0 \\ 0 & 0 & r & r & 0 & 0 & 0 \end{pmatrix}. \quad (\text{S3})$$

The corresponding eigenvalues and eigenvectors $E_n, |\psi_n\rangle = (c_{0,n}, c_{1,n}, c_{2,n}, c_{3,n}, c_{4,n}, c_{5,n}, c_{6,n})^T$ are as follows

$$E_0 = 0, \quad |\psi_0\rangle = \frac{1}{\sqrt{1+2r^2}} (0, 0, -r, r, 0, 0, 1)^T, \quad (\text{S4})$$

$$E_1 = 0, \quad |\psi_1\rangle = \frac{1}{\sqrt{2+2r^2}} (-1, 0, r, -r, 0, 1, 0)^T, \quad (\text{S5})$$

$$E_2 = 0, \quad |\psi_0\rangle = \frac{1}{\sqrt{4+1/r^2}} (-1/r, -1, 1, -1, 1, 0, 0)^T, \quad (\text{S6})$$

$$E_3 = -\sqrt{1+2r^2}, \quad |\psi_3\rangle = \frac{1}{\mathcal{N}} (0, \beta, -\alpha, -\beta, \alpha, -1, 1)^T, \quad (\text{S7})$$

$$E_4 = +\sqrt{1+2r^2}, \quad |\psi_4\rangle = \frac{1}{\mathcal{N}} (0, -\alpha, \beta, \alpha, -\beta, -1, 1)^T, \quad (\text{S8})$$

$$E_5 = -\sqrt{1+6r^2}, \quad |\psi_5\rangle = \frac{1}{\mathcal{N}'} (2, -\beta', -\alpha', -\beta', -\alpha', 1, 1)^T, \quad (\text{S9})$$

$$E_6 = +\sqrt{1+6r^2}, \quad |\psi_6\rangle = \frac{1}{\mathcal{N}'} (2, \alpha', \beta', \alpha', \beta', 1, 1)^T, \quad (\text{S10})$$

where we have introduced the following definitions

$$\alpha = \frac{1}{2r} (\sqrt{1+2r^2} - 1), \quad \beta = \frac{1}{2r} (\sqrt{1+2r^2} + 1), \quad \mathcal{N} = \sqrt{2}\sqrt{2+1/r^2} \quad (\text{S11})$$

$$\alpha' = \frac{1}{2r} (\sqrt{1+6r^2} - 1), \quad \beta' = \frac{1}{2r} (\sqrt{1+6r^2} + 1), \quad \mathcal{N}' = \sqrt{2}\sqrt{1+6/r^2}. \quad (\text{S12})$$

We note that there are three zero energy modes and the spectrum is symmetric around $E = 0$ as expected from general arguments given using the presence of chirality operator \mathcal{C} in the main text.

In what follows, we study the magnetization dynamics of the single plaquette. We first consider dynamics of the transverse magnetization starting from the $|\mathbb{Z}_2\rangle$ state. To this end, we note that $\hat{\sigma}_j^x$ for sites $j = 1, 2, 3, 4$, can be written in terms of the Fock states $\{|\mathcal{F}_\alpha\rangle, \alpha = 0, 1, \dots, 6\}$ as

$$\hat{\sigma}_1^x = (|\mathcal{F}_0\rangle \langle \mathcal{F}_1| + |\mathcal{F}_4\rangle \langle \mathcal{F}_5| + \text{h.c.}), \quad \hat{\sigma}_2^x = (|\mathcal{F}_0\rangle \langle \mathcal{F}_2| + |\mathcal{F}_3\rangle \langle \mathcal{F}_6| + \text{h.c.}) \quad (\text{S13})$$

$$\hat{\sigma}_3^x = (|\mathcal{F}_0\rangle \langle \mathcal{F}_3| + |\mathcal{F}_2\rangle \langle \mathcal{F}_6| + \text{h.c.}), \quad \hat{\sigma}_4^x = (|\mathcal{F}_0\rangle \langle \mathcal{F}_4| + |\mathcal{F}_5\rangle \langle \mathcal{F}_1| + \text{h.c.}) \quad (\text{S14})$$

To study the magnetization dynamics of a single plaquette, we now start from the $|\mathbb{Z}_2\rangle = |\mathcal{F}_5\rangle$ initial state and obtain the time dependent state $|\psi(t)\rangle = \sum_{\alpha=0..6} c_\alpha(t) |\mathcal{F}_\alpha\rangle$ by solving the Schrödinger equation

$$i \frac{dc_\alpha(t)}{dt} = \sum_{\beta=0..6} \langle \mathcal{F}_\alpha | H | \mathcal{F}_\beta \rangle c_\beta(t), \quad c_5(0) = 1, \quad c_{\alpha \neq 5}(0) = 0, \quad (\text{S15})$$

where we have scaled t in units of \hbar/w . Using $E_1 = w\sqrt{1+2r^2}$, $E_2 = w\sqrt{1+6r^2}$, we find

$$\begin{aligned} c_0(t) &= 2r^2(-1 + \cos E_2 t)/E_2^2 & c_1(t) &= \frac{r}{2} \left(\sum_{n=1,2} (1 - \cos E_n x)/E_n^2 - i \sin(E_n x)/E_n \right) = -c_5^*(t), \\ c_3(t) &= \frac{r}{2} \sum_{n=1,2} \left[2r^2/(E_1^2 E_2^2) + (-1)^n (\cos(E_1 t)/E_n^2 - i \sin(E_n x)/E_n) \right], = -c_4^*(t), \\ c_5(t) &= 1 - \frac{2r^2(1+4r^2)}{E_1^2 E_2^2} + r^2 \sum_{n=1,2} \cos(E_n x)/E_n^2, & c_6(t) &= \frac{-4r^2}{E_1^2 E_2^2} + r^2 \sum_{n=1,2} (-1)^n \cos(E_n x)/E_n^2. \end{aligned} \quad (\text{S16})$$

Next, we provide an approximate form for the time-dependent many-body wavefunction using $|\psi(t)\rangle$ given by (Fig. S2)

$$|\Psi(\{c^{(1)}\}, \{c^{(2)}\})\rangle(t) = |\Psi^{(1)}(c^{(1)})\rangle(t) + |\Psi^{(2)}(c^{(2)})\rangle(t), \quad (\text{S17})$$

$$|\Psi^{(1)}(c^{(1)})\rangle(t) = \bigotimes_{u=1,3,5,\dots} |\psi^{(1)}(c^{(1)})\rangle_u(t), \quad |\Psi^{(2)}(c^{(2)})\rangle(t) = \bigotimes_{u=2,4,6,\dots} |\psi^{(2)}(c^{(2)})\rangle_u(t), \quad (\text{S18})$$

$$|\psi^{(1,2)}(c^{(1,2)})\rangle_u(t) = \sum_{\alpha=0}^6 c_{\alpha}^{(1,2)}(t) |\mathcal{F}_{\alpha}\rangle_u. \quad (\text{S19})$$

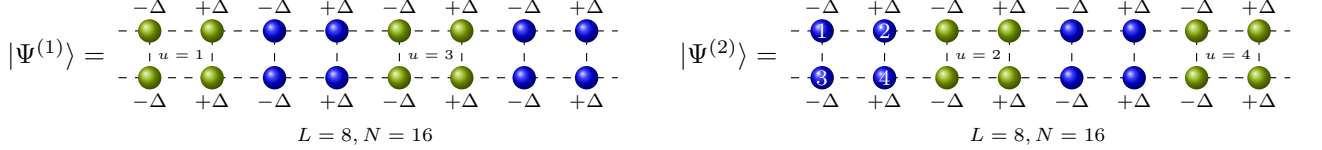


FIG. S2. Schematic representation of $|\psi^{(1,2)}\rangle$ for $N = 2L = 16$. The green sites represent dynamic spins while the blue sites represent spins frozen to $|\downarrow\rangle$.

In the above, the single plaquette Fock states, $\{|\mathcal{F}_{\alpha}\rangle, \alpha = 0, \dots, 6\}$ are replaced by the corresponding Fock states of the u -th plaquette (or unit cell) denoted as $\{|\mathcal{F}_{\alpha}\rangle_u, \alpha = 0, \dots, 6\}$. This is the simplest wavefunction in the total momentum $k_x = 0$ sector that reproduces exact dynamics at the level of a single plaquette; however, it can not capture inter-plaquette interaction which is key to thermalization. Nevertheless we show that several qualitative feature of the dynamics obtained from such a state reproduces several properties of the exact dynamics including the imbalance.

Using Eqs. S17 and S19, one can obtain analytic expression for $M_{j,a}^x(t) = \langle \psi(t) | \sigma_{ja}^x | \psi(t) \rangle / N$ for $j = 1..2$ and $a = 1, 2$. Note that for all other sites, within the approximate variational wavefunction, one obtains identical value of the magnetization. Using Eqs. (S19), (S16), and (S14), we find

$$\begin{aligned} M_{2,2}^x(t) &= -M_{1,1}^x(t) = \frac{1}{2} \left(\sum_{n=1,2} \cos(E_n x) / E_n^2 - 2 \frac{1+4r^2}{E_1^2 E_2^2} \right) \left(r^2 \sum_{n=1,2} (-1)^n \cos(E_n x) / E_n^2 + \frac{1+8r^2(1+r^2)}{2E_1^2 E_2^2} \right), \\ M_{2,1}^x(t) &= -M_{1,2}^x(t) = \frac{r^3}{2} \left(\sum_{n=1,2} \cos(E_n x) / E_n^2 - 2 \frac{1+4r^2}{E_1^2 E_2^2} \right) \left(\frac{4r^2}{E_1^2 E_2^2} - \sum_{n=1,2} (-1)^n \cos(E_n x) / E_n^2 \right). \end{aligned} \quad (\text{S20})$$

A plot of the transverse magnetization shown in Fig. S3 for $r = 1/2$ ($\Delta = 1 = w$). We note that it reproduces the qualitative structure of the dynamics obtained from exact numerics; in particular $|M_{1,2}^x| \ll M_{1,1}^x$ and $M_{1,a}^x = -M_{2,\bar{a}}^x$ at all times. Moreover, the steady state value of the transverse magnetization can be obtained from Eq. (S20) and yields, for the steady-state imbalance,

$$\mathcal{I}_{\mathbb{Z}_2}^x = M_{2,2}^{x \text{ steady}} + M_{2,1}^{x \text{ steady}} - M_{1,1}^{x \text{ steady}} - M_{1,2}^{x \text{ steady}} = \frac{r(1+4r^2)^3}{E_1^4 E_2^4}. \quad (\text{S21})$$

A plot of $\mathcal{I}_{\mathbb{Z}_2}^x$ is shown in the middle panel of Fig. S3. Note that $\mathcal{I}_{\mathbb{Z}_2}^x$ vanishes as $1/r$ for large r which reproduces its linear behavior around $\Delta \simeq 0$ as found in the main text. Also, it vanishes for $r \rightarrow 0$ ($\Delta/w \rightarrow \infty$) which can be understood by noting that in this limit the energy eigenstates become eigenstates of σ^z leading to vanishing of M^x on all sites. It is worth noting that for the initial states $|\psi(0)\rangle$ that belong to the $k_x = 0$ sector (such as $|\mathbb{Z}_2\rangle$ and $|\text{vac}\rangle$) the sign structure of the local magnetization found here agrees with that obtained from the exact numerics presented in the main text. In between, $\mathcal{I}_{\mathbb{Z}_2}^x$ peaks at $r = 1/\sqrt{2}$ or $\Delta = 1/\sqrt{2}$; the position of the peak do not agree with the numerical results which we find to be at $\Delta/w > 1$.

An exact similar calculation can be carried out for obtaining the dynamics of the longitudinal magnetization starting from the \mathbb{Z}_2 state. The computations are identical to those charted out before and we obtain, for $M_{j,a}^z(t) =$

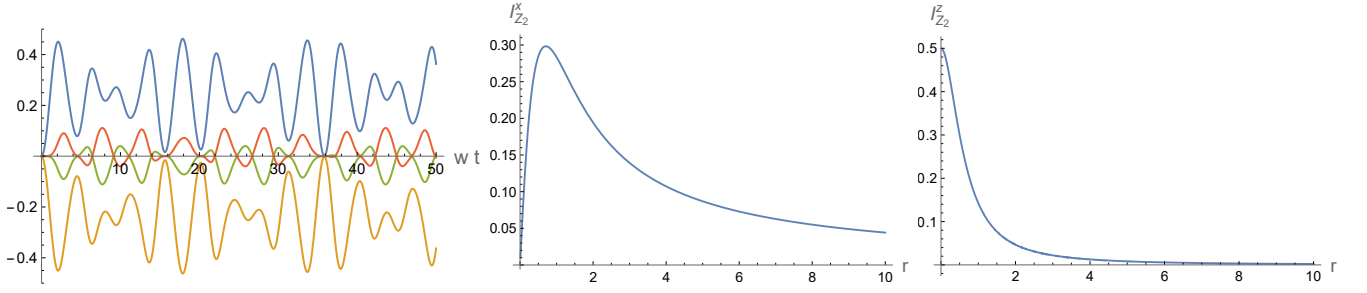


FIG. S3. Left Panel: Plot of $M_{2,2}^z(t)$ (blue), $M_{2,1}^x(t)$ (red), $M_{1,2}^x(t)$ (green) and $M_{1,1}^x(t)$ (yellow) as a function of wt showing $M_{1a}^x(t) = -M_{2a}^x(t)$ for all t . Middle Panel: Plot of the steady state transverse imbalance $\mathcal{I}_{Z_2}^x$ as a function of $r = w/(2\Delta)$. Right panel: Plot of $\mathcal{I}_{Z_2}^z$ as a function of $r = w/(2\Delta)$. For all plots $\hbar = 1$.

$\langle \psi(t) | \sigma_{j,a}^z | \psi(t) \rangle$,

$$\begin{aligned}
 M_{1,1}^z(t) &= M_{2,2}^z(t) = -\frac{1}{2} + \frac{r^2(1+4r^2)(5+40r^2+48r^4)}{4E_1^4E_2^4} + r^2 \left[\frac{\cos(2E_1t)}{4E_1^4} + \frac{\cos E_1t}{2E_1^4E_2^4} (2E_2^2(1+8r^2(1+r^2))) \right. \\
 &\quad \left. + E_1^2E_2^2(1+4r^2)\cos E_2t + \frac{4(E_1^2E_2^2-4r^2)\cos E_2t + r^2E_1^2\cos 2E_2t + 2E_1E_2^3\sin E_1t\sin E_2t}{4E_1^2E_2^4} \right], \quad (\text{S22}) \\
 M_{1,2}^z(t) &= M_{2,1}^z(t) = -\frac{1}{2} + \frac{r^2(1+12r^2+56r^4+96r^6)}{2E_1^4E_2^4} + \frac{r^2}{4E_1^4E_2^4} \left[(E_2^4\cos 2E_1t - 2(E_1^2E_2^2 + r^2E_2^2)) \right. \\
 &\quad \left. \times (4r^2 + E_1^2\cos E_2t)\cos E_1t + E_1^2(8r^2(E_1^2 + r^2)\cos E_2t - r^2E_1^2\cos 2E_2t - 2E_1E_2^3\sin E_1t\sin E_2t) \right].
 \end{aligned}$$

We note that this yields the same qualitative structure of the longitudinal matrix elements as from exact numerics and leads to a long-time imbalance given by

$$\mathcal{I}_{Z_2}^z = (M_{2,2}^{z \text{ steady}} + M_{1,1}^{z \text{ steady}} - M_{1,2}^{z \text{ steady}} - M_{2,1}^{z \text{ steady}}) = 2 \frac{1+5r^2}{E_1^2E_2^2}. \quad (\text{S23})$$

Note that for $r = 0$, $|Z_2\rangle$ is an eigenstate and hence the long-time value of the imbalance is close to its value 2 in the initial state. In contrast, $\mathcal{I}_{Z_2}^z$ vanishes as $1/r^2$ in the large r limit which explain its quadratic behavior around $\Delta \rightarrow 0$; this also shows that the imbalance is absent in the standard PXP chain for which $\Delta = 0$.

Finally, we consider the $|\text{vac}\rangle$ initial state. To this end, we once again solve Eq. (S15) but with initial condition $c_0(0) = 1$ and $c_\alpha(0) = 0$ for $\alpha \neq 0$. The wavefunction for the single plaquette, at any time t , can be written as $|\psi(t)\rangle = \sum_{\alpha=0..6} d_\alpha(t) |\mathcal{F}_\alpha\rangle$, where $d_\alpha(t)$ is given by

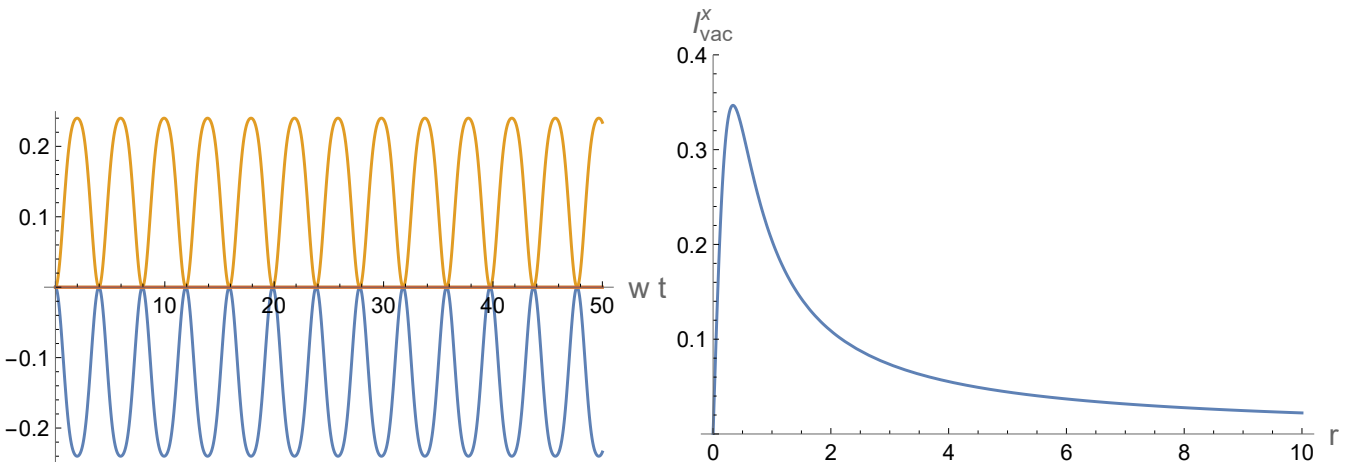


FIG. S4. Left Panel: Plot of $M_{2,2}^x(t)$ and $M_{1,1}^x(t)$ as a function of wt . Right Panel: Plot of the steady state imbalance $\mathcal{I}_{\text{vac}}^x$ as a function of $r = w/(2\Delta)$. For all plots $\hbar = 1$.

$$\begin{aligned}
d_0(t) &= \frac{E_1^2 + r^2 \cos E_2 t}{E_2^2}, & d_1(t) = -d_2^*(t) = d_3(t) = -d_4^*(t) &= \frac{r(\cos E_2 t - 1 - iE_2 \sin E_2 t)}{E_2^2}, \\
d_5(t) &= d_6(t) = \frac{2r^2(\cos E_2 t - 1)}{E_2^2}.
\end{aligned} \tag{S24}$$

Using Eq. (S24), one can easily obtain the transverse and longitudinal magnetizations for the vacuum states. For the longitudinal magnetization, we find the longitudinal magnetization is same for all sites and is given by

$$M_{\text{vac}}^z(t) = -\frac{1}{2E_2^2} + \frac{r^2}{E_2^4} (1 - \cos E_2 t). \tag{S25}$$

In contrast for the transverse magnetization, one finds $M_{2,1}^x = M_{2,2}^x = -M_{1,1}^x = -M_{1,2}^x = M_{\text{vac}}^x(t)$ at all times where

$$M_{\text{vac}}^x(t) = \frac{r(\cos E_2 t - 1)(E_2^2 + 4r^2(\cos E_2 t - 1))}{E_2^4}. \tag{S26}$$

This is shown in the left panel of Fig. S4 and leads to a long-time imbalance,

$$\mathcal{I}_{\text{vac}}^x = \frac{2r(1 + 4r^2)}{(1 + 6r^2)^2}, \tag{S27}$$

as shown in the right panel of Fig. S4. The imbalance vanishes both at $r = 0$ and $r \rightarrow \infty$; the latter shows absence of such imbalance in the pure PXP chain. However, this simplistic model does not reproduce the feature that the imbalance grows from around $\Delta \sim 0.5$; instead it shows a linear growth around $\Delta = 0$. This is most likely due to the effect of inter-plaquette interaction ignored in this simplistic model and is beyond the scope of the current analysis.

S4. CHIRALITY OPERATORS AND SPECTRAL REFLECTION SYMMETRY

In this section, we demonstrate the existence of two chirality operators $\hat{C}_{1,2}$ that satisfy $\hat{C}_{1,2}|E_\mu\rangle = |-E_\mu\rangle$ for any finite $E_\mu \neq 0$. To this end, we consider the chirality operator $\prod_i \hat{\sigma}_i^z$ of the PXP chain, generalized to the case of a ladder geometry, and define the operators \hat{C}_1 and \hat{C}_2 using translations as follows

$$\hat{C} = \prod_{j=1}^L \prod_{a=1}^2 \hat{\sigma}_{j,a}^z, \quad \hat{C}_1 = \hat{T}_x \hat{C}, \quad \hat{C}_2 = \hat{T}_x \hat{T}_y \hat{C}. \tag{S28}$$

We set the convention that, the action of translation operators $\hat{T}_{x,y}$, on a Fock state translates the spin pattern by one unit to the positive x/y direction. Evidently, the operators \hat{C}_1 and \hat{C}_2 have the following properties

$$\{\hat{C}_1, \hat{\mathcal{H}}\} = \{\hat{C}_2, \hat{\mathcal{H}}\} = 0. \tag{S29}$$

To see this consider $\hat{C}_2^{-1} \hat{\mathcal{H}} \hat{C}_2$

$$\hat{C}_2^{-1} \hat{\mathcal{H}} \hat{C}_2 = \hat{C}^{-1} \hat{T}_y^{-1} \hat{T}_x^{-1} (\hat{\mathcal{H}}_z + \hat{\mathcal{H}}_x) \hat{T}_x \hat{T}_y \hat{C} = -\hat{\mathcal{H}}_z - \hat{\mathcal{H}}_x = -\hat{\mathcal{H}}, \tag{S30}$$

where we have used the fact that

$$\begin{aligned}
\hat{T}_x^{-1} \hat{\mathcal{H}}_z \hat{T}_x &= -\hat{\mathcal{H}}_z, & \hat{T}_y^{-1} \hat{\mathcal{H}}_z \hat{T}_y &= \hat{\mathcal{H}}_z, & \hat{C}^{-1} \hat{\mathcal{H}}_z \hat{C} &= \hat{\mathcal{H}}_z, \\
\hat{T}_x^{-1} \hat{\mathcal{H}}_x \hat{T}_x &= \hat{\mathcal{H}}_x, & \hat{T}_y^{-1} \hat{\mathcal{H}}_x \hat{T}_y &= \hat{\mathcal{H}}_x, & \hat{C}^{-1} \hat{\mathcal{H}}_x \hat{C} &= -\hat{\mathcal{H}}_x.
\end{aligned} \tag{S31}$$

This establishes Eq. (S29) for \hat{C}_2 ; a similar proof can be easily obtained for \hat{C}_1 .

Eqs. (S29) implies that the operators \hat{C}_1 and \hat{C}_2 are indeed chirality operators. This means that if $|E_\mu\rangle$ is an eigenmode of $\hat{\mathcal{H}}$ with eigenvalue E_μ , then $\hat{C}_{1,2}|E_\mu\rangle$ is also an eigenvector of $\hat{\mathcal{H}}$ but with eigenvalue $-E_\mu$. Thus the Hamiltonian $\hat{\mathcal{H}}$ has reflection symmetry for $\Delta \neq 0$. Moreover, if $\hat{C}_{1,2}|E_\mu\rangle$ is a normalized vector then we can identify it with $|-E_\mu\rangle$ for $E_\mu \neq 0$ up to an overall sign. The situations for the zero modes have further subtleties and shall be addressed later. For $E_\mu \neq 0$, we find

$$\|\hat{C}_1 |E_\mu\rangle\| = \langle E_\mu | \hat{C}_1^\dagger \hat{C}_1 |E_\mu\rangle = \langle E_\mu | \hat{C}_1^{-1} \hat{C}_1 |E_\mu\rangle = 1. \tag{S32}$$

In the above derivation we have used the relation $\hat{\mathcal{C}}_1^\dagger = \hat{\mathcal{C}}_1^{-1}$ which can be shown as follows

$$\hat{\mathcal{C}}_1^\dagger = (\hat{T}_x \hat{\mathcal{C}})^\dagger = \hat{\mathcal{C}}^\dagger \hat{T}_x^\dagger = \hat{\mathcal{C}}^\dagger \hat{T}_x^{-1} = \hat{\mathcal{C}}^{-1} \hat{T}_x^{-1} = (\hat{T}_x \hat{\mathcal{C}})^{-1} = \hat{\mathcal{C}}_1^{-1}. \quad (\text{S33})$$

Thus we find that $\hat{\mathcal{C}}_1 |E_\mu\rangle = |-E_\mu\rangle$; similar arguments for $\hat{\mathcal{C}}_2$ shows $\hat{\mathcal{C}}_2 |E_\mu\rangle = |-E_\mu\rangle$. We shall use these properties in the next subsection to derive properties of the imbalance operators. We further note that both $\hat{\mathcal{C}}_1$ and $\hat{\mathcal{C}}_2$ as well as the Hamiltonian $\hat{\mathcal{H}}$ commute with $\hat{\mathcal{R}}_x$, where $\hat{\mathcal{R}}_x$ denotes a reflection of sites along an axis that is perpendicular to the rungs and exchanges the two sites of each rung. This intertwining of the chirality and reflection symmetry leads to an exponentially large number (in system size) of exact mid-spectrum zero modes with $E = 0$ due to the index theorem referred to in the main text.

S5. DERIVATION OF SOME EXACT ASPECTS

In this section, we provide some exact analytical results which supports the numerical observations regarding the dynamics of site resolved magnetizations and the long-time average values of the imbalance operators mentioned in the main text. Our results explain why only the zero modes of the Hamiltonian contribute to the infinite time average values of imbalances $\hat{I}_{|\mathbb{Z}_2}^z$ and $\hat{I}_{|\mathbb{Z}_2}^x$, while for $\hat{I}_{|\text{vac}}^x$ both zero modes and non-zero modes may contribute in general. We show that this property in turn relies on the relations amongst site-resolved magnetizations $\langle \hat{\sigma}_{i,a}^z \rangle$ and $\langle \hat{\sigma}_{i,a}^x \rangle$ for sites $i = 1, 2$ and $a = 1, 2$. We also provide, by using the various properties of the two chirality operators $\hat{\mathcal{C}}_1, \hat{\mathcal{C}}_2$ introduced in Sec. S4, an analytic derivation of these exact aspects observed in numerical analysis previously.

A. Long-time average values of imbalance operators $\hat{I}_{|\mathbb{Z}_2}^z$ and $\hat{I}_{|\mathbb{Z}_2}^x$

In this section, we consider the implications of the presence of the two chirality operators for long-time average imbalances. First we note that the diagonal and off diagonal matrix elements of $\hat{\sigma}_{i,a}^z$ operators in the space of non-zero eigenmodes of the Hamiltonian $\hat{\mathcal{H}}$ are related to each other due to these chirality operators $\hat{\mathcal{C}}_{1,2}$. This can be seen from the relations

$$\begin{aligned} \langle E_\mu | \hat{\sigma}_{i,a}^z | E_\nu \rangle &= \langle E_\mu | \hat{\mathcal{C}}_1^{-1} \hat{\mathcal{C}}_1 \hat{\sigma}_{i,a}^z \hat{\mathcal{C}}_1^{-1} \hat{\mathcal{C}}_1 | E_\nu \rangle = \langle E_\mu | \hat{\mathcal{C}}_1^\dagger (\hat{\mathcal{C}}_1 \hat{\sigma}_{i,a}^z \hat{\mathcal{C}}_1^{-1}) \hat{\mathcal{C}}_1 | E_\nu \rangle = \langle -E_\mu | (\hat{T}_x \hat{\mathcal{C}} \hat{\sigma}_{i,a}^z \hat{\mathcal{C}}^{-1} \hat{T}_x^{-1}) | -E_\nu \rangle \\ &= \langle -E_\mu | (\hat{T}_x \hat{\sigma}_{i,a}^z \hat{T}_x^{-1}) | -E_\nu \rangle = \langle -E_\mu | \hat{\sigma}_{i+1,a}^z | -E_\nu \rangle. \end{aligned} \quad (\text{S34})$$

Similarly using the operator \mathcal{C}_2 , one obtains

$$\langle E_\mu | \hat{\sigma}_{i,a}^z | E_\nu \rangle = \langle -E_\mu | \hat{\sigma}_{i+1,\bar{a}}^z | -E_\nu \rangle. \quad (\text{S35})$$

It is worthwhile to note that these relations do not hold in a similar manner for the zero modes for which $\hat{\mathcal{C}}_q |\Phi_{\mu_0}\rangle = |\Phi_{\mu_0}^*\rangle$. Since the set zero modes $\{|\Phi_{\mu_0}\rangle, \mu_0 = 1, 2, \dots, \mathcal{N}_0\}$ form an orthonormal (albeit degenerate) subspace of eigenvectors, it is easy to see that the modified set of zero modes $\{\hat{\mathcal{C}}_q |\Phi_{\mu_0}\rangle, \mu_0 = 1, 2, \dots, \mathcal{N}_0\} = \{|\Phi_{\mu_0}^*\rangle, \mu_0 = 1, 2, \dots, \mathcal{N}_0\}$ are also a set of orthonormal set of degenerate eigenvectors of $\hat{\mathcal{H}}$. This can be understood by considering the inner product between two vectors from this modified set. Since $\langle \Phi_{\mu_0} | \Phi_{\nu_0} \rangle = \delta_{\mu_0, \nu_0}$, we have

$$\langle \Phi_{\mu_0}^* | \Phi_{\nu_0}^* \rangle = \langle \Phi_{\mu_0} | \hat{\mathcal{C}}_q^\dagger \hat{\mathcal{C}}_q | \Phi_{\nu_0} \rangle = \langle \Phi_{\mu_0} | \hat{\mathcal{C}}_q^{-1} \hat{\mathcal{C}}_q | \Phi_{\nu_0} \rangle = \delta_{\mu_0, \nu_0}. \quad (\text{S36})$$

An analysis similar to that in Eq. (S34) then leads to

$$\langle \Phi_{\mu_0} | \hat{\sigma}_{i,a}^z | \Phi_{\nu_0} \rangle = \langle \Phi_{\mu_0} | \hat{\mathcal{C}}_q^{-1} \hat{\mathcal{C}}_q \hat{\sigma}_{i,a}^z \hat{\mathcal{C}}_q^{-1} \hat{\mathcal{C}}_q | \Phi_{\nu_0} \rangle = \langle \Phi_{\mu_0} | \hat{\mathcal{C}}_q^\dagger (\hat{\mathcal{C}}_q \hat{\sigma}_{i,a}^z \hat{\mathcal{C}}_q^{-1}) \hat{\mathcal{C}}_q | \Phi_{\nu_0} \rangle = \langle \Phi_{\mu_0}^* | (\hat{\mathcal{C}}_q \hat{\sigma}_{i,a}^z \hat{\mathcal{C}}_q^{-1}) | \Phi_{\nu_0}^* \rangle. \quad (\text{S37})$$

For $q = 1, 2$ one thus obtains

$$\langle \Phi_{\mu_0} | \hat{\sigma}_{i,a}^z | \Phi_{\nu_0} \rangle = \langle \Phi_{\mu_0}^* | \hat{\sigma}_{i+1,a}^z | \Phi_{\nu_0}^* \rangle = \langle \Phi_{\mu_0}^* | \hat{\sigma}_{i,\bar{a}}^z | \Phi_{\nu_0}^* \rangle. \quad (\text{S38})$$

Let us consider the dynamical consequences of Eqs. (S34) and (S35). A quench from an initial state $|\psi(0)\rangle$ leads to the instantaneous expectation value of $\hat{\sigma}_{i,a}^z$ with respect to the quantum state $|\psi(t)\rangle$ at time t reads

$$\langle \hat{\sigma}_{i,a}^z(t) \rangle = \sum_{\mu=1}^{\mathcal{D}_H} \sum_{\nu=1}^{\mathcal{D}_H} \langle \psi(0) | E_\mu \rangle (\hat{\sigma}_{i,a}^z)_{\mu\nu} \langle E_\nu | \psi(0) \rangle e^{i\omega_{\mu\nu} t}. \quad (\text{S39})$$

Here we have introduced the notation $\omega_{\mu\nu} = (E_\mu - E_\nu)/\hbar$ and $(\cdot)_{\mu\nu} = \langle E_\mu | \cdot | E_\nu \rangle$. The *infinite time average* of $\langle \hat{\sigma}_{i,a}^z(t) \rangle$ is

$$\overline{\hat{\sigma}_{i,a}^z} = \lim_{T \rightarrow \infty} \frac{1}{T} \int_0^T dt \langle \hat{\sigma}_{i,a}^z(t) \rangle = \sum_{\mu \notin \mathcal{H}_0} |\langle \psi(0) | E_\mu \rangle|^2 (\hat{\sigma}_{i,a}^z)_{\mu\mu} + \sum_{\mu \in \mathcal{H}_0} \sum_{\nu \in \mathcal{H}_0} \langle \psi(0) | E_\mu \rangle \langle E_\nu | \psi(0) \rangle (\hat{\sigma}_{i,a}^z)_{\mu\nu}. \quad (\text{S40})$$

For the specific initial states considered in the main text, one has

$$\langle \psi(0) | \hat{\mathcal{H}} | \psi(0) \rangle = \sum_{\mu=1}^{\mathcal{D}_H} E_\mu |\langle \psi(0) | E_\mu \rangle|^2 = \sum_{\mu \notin \mathcal{H}_0} E_\mu |\langle \psi(0) | E_\mu \rangle|^2 = 0. \quad (\text{S41})$$

This implies that for these initial states, overlap of the initial state with the non-zero modes, i.e. $\{|E_\mu\rangle, \mu \notin \mathcal{H}_0\}$ satisfies the relation

$$|\langle \psi(0) | E_\mu \rangle|^2 = |\langle \psi(0) | -E_\mu \rangle|^2, \quad \forall E_\mu > 0. \quad (\text{S42})$$

From Eq. (S42) and Eq. (S34), by setting $\mu = \nu$, we can see that

$$\sum_{\mu \notin \mathcal{H}_0} |\langle \psi(0) | E_\mu \rangle|^2 (\hat{\sigma}_{i,a}^z)_{\mu\mu} = \sum_{\mu \notin \mathcal{H}_0} |\langle \psi(0) | E_\mu \rangle|^2 (\hat{\sigma}_{i+1,a}^z)_{\mu\mu}. \quad (\text{S43})$$

This shows that the contribution to infinite time average from non-zero modes for operators $\hat{\sigma}_{i,a}^z$ and $\hat{\sigma}_{i+1,a}^z$ are identical. This immediately implies that the imbalance $\hat{\mathcal{I}}_{|\mathbb{Z}_2}^z$ does not have any contribution from the sector of non-zero energy eigenmodes as it is defined by

$$\hat{\mathcal{I}}_{|\mathbb{Z}_2}^z = \frac{1}{L} \sum_{r=1}^{L/2} \hat{T}_x^{2r} (\hat{\sigma}_{1,1}^z - \hat{\sigma}_{2,1}^z - \hat{\sigma}_{1,2}^z + \hat{\sigma}_{2,2}^z). \quad (\text{S44})$$

Using Eq. (S43) therefore leads to

$$\sum_{\mu \notin \mathcal{H}_0} |\langle \psi(0) | E_\mu \rangle|^2 (\hat{\mathcal{I}}_{|\mathbb{Z}_2}^z)_{\mu\mu} = 0. \quad (\text{S45})$$

Note that a similar analysis for the zero modes lead to a possibility of non-zero contribution to the imbalance; this can happen if one or few of these modes have larger overlap with the initial state than the rest. In our numerics, we find that this is indeed the case.

Next we carry out a similar analysis for the matrix elements of $\hat{\sigma}_{i,a}^x$. This yields, using \mathcal{C}_1 ,

$$\begin{aligned} \langle E_\mu | \hat{\sigma}_{i,a}^x | E_\nu \rangle &= \langle E_\mu | \hat{\mathcal{C}}_1^{-1} \hat{\mathcal{C}}_1 \hat{\sigma}_{i,a}^x \hat{\mathcal{C}}_1^{-1} \hat{\mathcal{C}}_1 | E_\nu \rangle = \langle E_\mu | \hat{\mathcal{C}}_1^\dagger \left(\hat{T}_x \hat{\mathcal{C}} \hat{\sigma}_{i,a}^x \hat{\mathcal{C}}^{-1} \hat{T}_x^{-1} \right) \hat{\mathcal{C}}_1 | E_\nu \rangle \\ &= -\langle -E_\mu | \left(\hat{T}_x \hat{\sigma}_{i,a}^x \hat{T}_x^{-1} \right) | -E_\nu \rangle = -\langle -E_\mu | \hat{\sigma}_{i+1,a}^x | -E_\nu \rangle. \end{aligned} \quad (\text{S46})$$

Similarly using \mathcal{C}_2 , we obtain

$$\langle E_\mu | \hat{\sigma}_{i,a}^x | E_\nu \rangle = -\langle -E_\mu | \hat{\sigma}_{i+1,\bar{a}}^x | -E_\nu \rangle. \quad (\text{S47})$$

The matrix elements for the zero mode sectors can also be obtained in an identical manner and yields

$$\langle \Phi_{\mu_0} | \hat{\sigma}_{i,a}^x | \Phi_{\nu_0} \rangle = -\langle \Phi_{\mu_0}^* | \hat{\sigma}_{i+1,a}^x | \Phi_{\nu_0}^* \rangle = -\langle \Phi_{\mu_0}^* | \hat{\sigma}_{i,\bar{a}}^x | \Phi_{\nu_0}^* \rangle. \quad (\text{S48})$$

Using Eq. (S42) we find

$$\sum_{\mu \notin \mathcal{H}_0} |\langle \psi(0) | E_\mu \rangle|^2 (\hat{\sigma}_{i,a}^x)_{\mu\mu} = - \sum_{\mu \notin \mathcal{H}_0} |\langle \psi(0) | E_\mu \rangle|^2 (\hat{\sigma}_{i+1,a}^x)_{\mu\mu}. \quad (\text{S49})$$

Eq. (S49) shows that the contribution to infinite time average from non-zero modes for operators $\hat{\sigma}_{i,a}^x$ and $\hat{\sigma}_{i+1,a}^x$ are exactly opposite. This immediately implies that the imbalance $\hat{\mathcal{I}}_{|\mathbb{Z}_2}^x$ does not have any contribution from the sector non-zero energy eigenmodes. To see this more clearly we note that $\hat{\mathcal{I}}_{|\mathbb{Z}_2}^x$ is defined by

$$\hat{\mathcal{I}}_{|\mathbb{Z}_2}^x = \frac{1}{L} \sum_{r=1}^{L/2} \hat{T}_x^{2r} (-\hat{\sigma}_{1,1}^x - \hat{\sigma}_{2,1}^x + \hat{\sigma}_{1,2}^x + \hat{\sigma}_{2,2}^x). \quad (\text{S50})$$

Using Eq. (S49), one finds

$$\sum_{\mu \notin \mathcal{K}_0} |\langle \psi(0) | E_\mu \rangle|^2 (\hat{\mathcal{I}}_{|\mathbb{Z}_2\rangle}^x)_{\mu\mu} = 0. \quad (\text{S51})$$

Thus our results indicate that the long-time average imbalance found in the main text starting from the $|\mathbb{Z}_2\rangle$ state receives its contribution only from the zero-energy eigenstates. Before ending this section, we note that the imbalance operator $\hat{\mathcal{I}}_{|\text{vac}\rangle}^x$ is defined as

$$\hat{\mathcal{I}}_{|\text{vac}\rangle}^x = \frac{1}{L} \sum_{r=1}^{L/2} \hat{T}_x^{2r} (\hat{\sigma}_{1,1}^x + \hat{\sigma}_{1,2}^x - \hat{\sigma}_{2,1}^x - \hat{\sigma}_{2,2}^x), \quad (\text{S52})$$

and therefore its contribution does not necessarily vanish from the non-zero eigenmode sector (Eqs. (S46) and (S49)). In fact numerically, we find that it does receive contribution from both the zero- and non-zero mode sectors.

B. Instantaneous site-resolved magnetizations $\langle \hat{\sigma}_{i,a}^z \rangle_t$ and $\langle \hat{\sigma}_{i,a}^x \rangle_t$

The goal in this section is to investigate the reason behind some exact relations amongst the site resolved magnetization which are observed in the numerical results of quench dynamics. From the evolution of various site resolved magnetizations in the main text, we can find that the following relations hold for the $|\psi(0)\rangle = |\mathbb{Z}_2\rangle$ initial state, for any value of Δ

$$\langle \hat{\sigma}_{1,1}^z \rangle_t = \langle \hat{\sigma}_{2,2}^z \rangle_t, \quad \langle \hat{\sigma}_{1,2}^z \rangle_t = \langle \hat{\sigma}_{2,1}^z \rangle_t, \quad \langle \hat{\sigma}_{1,1}^x \rangle_t = -\langle \hat{\sigma}_{2,2}^x \rangle_t, \quad \langle \hat{\sigma}_{1,2}^x \rangle_t = -\langle \hat{\sigma}_{2,1}^x \rangle_t, \quad (\text{S53a})$$

whereas for $|\psi(0)\rangle = |\text{vac}\rangle$ initial state we find

$$\langle \hat{\sigma}_{1,1}^z \rangle_t = \langle \hat{\sigma}_{2,2}^z \rangle_t = \langle \hat{\sigma}_{1,2}^z \rangle_t = \langle \hat{\sigma}_{2,1}^z \rangle_t, \quad \langle \hat{\sigma}_{1,1}^x \rangle_t = \langle \hat{\sigma}_{1,2}^x \rangle_t = -\langle \hat{\sigma}_{2,2}^x \rangle_t = -\langle \hat{\sigma}_{2,1}^x \rangle_t. \quad (\text{S54a})$$

In the following we shall explore the underlying reason for these equalities during quench dynamics. For this purpose, we first rewrite time dependence of magnetization $\hat{\sigma}_{i,a}^z$ as

$$\begin{aligned} \langle \hat{\sigma}_{i,a}^z \rangle(t) = & \underbrace{\sum_{\mu_0, \nu_0} \langle \psi(0) | \Phi_{\mu_0} \rangle \langle \Phi_{\nu_0} | \psi(0) \rangle (\hat{\sigma}_{i,a}^z)_{\mu_0 \nu_0}}_{\text{I}} + \underbrace{\sum_{\mu_0, \nu} \langle \psi(0) | \Phi_{\mu_0} \rangle \langle E_\nu | \psi(0) \rangle (\hat{\sigma}_{i,a}^z)_{\mu_0 \nu} e^{-iE_\nu t}}_{\text{II}} \\ & + \underbrace{\sum_{\mu, \nu} \langle \psi(0) | E_\mu \rangle \langle E_\nu | \psi(0) \rangle (\hat{\sigma}_{i,a}^z)_{\mu \nu} e^{+i(E_\mu - E_\nu)t}}_{\text{III}}. \end{aligned} \quad (\text{S55})$$

Here we have used the convention that $|E_\mu\rangle$ stands for the non-zero modes of the Hamiltonian with energy eigenvalue E_μ and $|\Phi_{\mu_0}\rangle$ denotes the zero modes of the Hamiltonian.

Eq. (S55) consists of three distinct parts. The first part (denoted by I) comes entirely from zero modes whereas the third part (III) comes entirely from non-zero modes. In contrast, part II receives contribution from both zero and non-zero modes. To analyze these contributions, we first focus on part III of the above partition. We recall from Sec. S5 A (for example Eqs. (S34) and (S35)) that for two non-zero modes $|E_\mu\rangle$ and $|E_\nu\rangle$ we have $\langle E_\mu | \hat{\sigma}_{i,a}^z | E_\nu \rangle = \langle -E_\mu | \hat{\sigma}_{i+1,a}^z | -E_\nu \rangle = \langle -E_\mu | \hat{\sigma}_{i+1,\bar{a}}^z | -E_\nu \rangle$. Moreover, the spectral reflection symmetry induced by the chirality operators $\hat{\mathcal{C}}_q$ ($q = 1, 2$) also allows us to relate $\langle \psi(0) | E_\mu \rangle$ and $\langle \psi(0) | -E_\mu \rangle$. To see this we note that

$$\langle \psi(0) | -E_\mu \rangle = \langle \psi(0) | \hat{\mathcal{C}}_q | E_\mu \rangle, \quad \langle \psi(0) | \hat{\mathcal{C}}_q = (\hat{\mathcal{C}}_q^\dagger | \psi(0) \rangle)^\dagger, \quad (\text{S56})$$

and consider for $|\psi(0)\rangle = |\text{vac}\rangle$ leading to

$$\begin{aligned} \langle \text{vac} | \hat{\mathcal{C}}_1 = (\hat{\mathcal{C}}_1^\dagger | \text{vac} \rangle)^\dagger &= (\hat{\mathcal{C}}^\dagger \hat{T}_x^\dagger | \text{vac} \rangle)^\dagger = (\hat{\mathcal{C}} \hat{T}_x^{-1} | \text{vac} \rangle)^\dagger = ((-1)^{N_{\text{sites}}} | \text{vac} \rangle)^\dagger = \langle \text{vac} |, \\ \langle \text{vac} | \hat{\mathcal{C}}_2 = (\hat{\mathcal{C}}_2^\dagger | \text{vac} \rangle)^\dagger &= (\hat{\mathcal{C}}^\dagger \hat{T}_x^\dagger \hat{T}_y^\dagger | \text{vac} \rangle)^\dagger = (\hat{\mathcal{C}} \hat{T}_x^{-1} \hat{T}_y^{-1} | \text{vac} \rangle)^\dagger = ((-1)^{N_{\text{sites}}} | \text{vac} \rangle)^\dagger = \langle \text{vac} |. \end{aligned}$$

For $|\psi(0)\rangle = |\mathbb{Z}_2\rangle$ we have

$$\begin{aligned} \langle \mathbb{Z}_2 | \hat{C}_1 &= (\hat{C}_1^\dagger |\mathbb{Z}_2\rangle)^\dagger = (\hat{C}^\dagger \hat{T}_x^\dagger |\mathbb{Z}_2\rangle)^\dagger = (\hat{C} \hat{T}_x^{-1} |\mathbb{Z}_2\rangle)^\dagger = ((-1)^{N_{\text{sites}}/2} |\overline{\mathbb{Z}_2}\rangle)^\dagger = |\overline{\mathbb{Z}_2}\rangle, \\ \langle \mathbb{Z}_2 | \hat{C}_2 &= (\hat{C}_2^\dagger |\mathbb{Z}_2\rangle)^\dagger = (\hat{C}^\dagger \hat{T}_x^\dagger \hat{T}_y^\dagger |\mathbb{Z}_2\rangle)^\dagger = (\hat{C} \hat{T}_x^{-1} \hat{T}_y^{-1} |\mathbb{Z}_2\rangle)^\dagger = ((-1)^{N_{\text{sites}}/2} |\mathbb{Z}_2\rangle)^\dagger = \langle \mathbb{Z}_2|. \end{aligned}$$

Using Eqs. (S34), (S35), (S38) along with Eq. (S57) to obtain the properties of instantaneous magnetization starting from the $|\mathbb{Z}_2\rangle$ state. To this end, we first consider $\langle \hat{\sigma}_{i,a}^z \rangle_{\mathbb{Z}_2}(t)$. The contribution to it from the $E = 0$ sector is given by

$$\langle \hat{\sigma}_{i,a}^z \rangle_{\mathbb{Z}_2}^{\text{I}}(t) = \sum_{\mu_0 \nu_0} \langle \Phi_{\mu_0} | \hat{\sigma}_{i,a}^z | \Phi_{\nu_0} \rangle \langle \Phi_{\nu_0} | \mathbb{Z}_2 \rangle \langle \mathbb{Z}_2 | \Phi_{\mu_0} \rangle = \sum_{\mu_0 \nu_0} \langle \Phi_{\mu_0}^* | \hat{\sigma}_{i+1,\bar{a}}^z | \Phi_{\nu_0}^* \rangle \langle \Phi_{\nu_0}^* | \mathbb{Z}_2 \rangle \langle \mathbb{Z}_2 | \Phi_{\mu_0}^* \rangle = \langle \hat{\sigma}_{i+1,\bar{a}}^z \rangle_{\mathbb{Z}_2}^{\text{I}}(t). \quad (\text{S57})$$

In addition, utilizing the \hat{C}_2 operator ($|\Phi_{\mu_0}^*\rangle = \hat{C}_2 |\Phi_{\mu_0}\rangle$), the cross terms which receives contribution from both the zero and the non-zero energy sectors can be shown to satisfy

$$\langle \hat{\sigma}_{i,a}^z \rangle_{\mathbb{Z}_2}^{\text{II}}(t) = \sum_{\mu_0 \nu} \langle \Phi_{\mu_0} | \hat{\sigma}_{i,a}^z | E_\nu \rangle \langle E_\nu | \mathbb{Z}_2 \rangle \langle \mathbb{Z}_2 | \Phi_{\mu_0} \rangle e^{-iE_\nu t} = \sum_{\mu_0 \nu} \langle \Phi_{\mu_0}^* | \hat{\sigma}_{i+1,\bar{a}}^z - E_\nu \rangle \langle -E_\nu | \mathbb{Z}_2 \rangle \langle \mathbb{Z}_2 | \Phi_{\mu_0}^* \rangle e^{-iE_\nu t} = \langle \hat{\sigma}_{i+1,\bar{a}}^z \rangle_{\mathbb{Z}_2}^{\text{II}}(t). \quad (\text{S58})$$

Moreover, the contribution from the non-zero energy sector yields

$$\begin{aligned} \langle \hat{\sigma}_{i,a}^z \rangle_{\mathbb{Z}_2}^{\text{III}}(t) &= \sum_{\mu\nu} \langle E_\mu | \hat{\sigma}_{i,a}^z | E_\nu \rangle \langle E_\nu | \mathbb{Z}_2 \rangle \langle \mathbb{Z}_2 | \Phi_{\mu_0} \rangle e^{i(E_\mu - E_\nu)t} \\ &= \sum_{\mu\nu} \langle -E_\mu | \hat{\sigma}_{i+1,\bar{a}}^z - E_\nu \rangle \langle -E_\nu | \mathbb{Z}_2 \rangle \langle \mathbb{Z}_2 | -E_\mu \rangle e^{i(E_\mu - E_\nu)t} = \langle \hat{\sigma}_{i+1,\bar{a}}^z \rangle_{\mathbb{Z}_2}^{\text{III}}(t). \end{aligned} \quad (\text{S59})$$

From the above equations we can therefore conclude that

$$\langle \hat{\sigma}_{i,a}^z \rangle_{\text{vac}}(t) = \langle \hat{\sigma}_{i+1,\bar{a}}^z \rangle_{\mathbb{Z}_2}(t). \quad (\text{S60})$$

Next, we Consider $\langle \hat{\sigma}_{i,a}^x \rangle_{\mathbb{Z}_2}(t)$. Using Eqs. (S46), (S47), (S48), we find, for the contribution to these matrix elements from the zero-energy sector

$$\langle \hat{\sigma}_{i,a}^x \rangle_{\mathbb{Z}_2}^{\text{I}}(t) = \sum_{\mu_0 \nu_0} \langle \Phi_{\mu_0} | \hat{\sigma}_{i,a}^x | \Phi_{\nu_0} \rangle \langle \Phi_{\nu_0} | \mathbb{Z}_2 \rangle \langle \mathbb{Z}_2 | \Phi_{\mu_0} \rangle = - \sum_{\mu_0 \nu_0} \langle \Phi_{\mu_0}^* | \hat{\sigma}_{i+1,\bar{a}}^x | \Phi_{\nu_0}^* \rangle \langle \Phi_{\nu_0}^* | \mathbb{Z}_2 \rangle \langle \mathbb{Z}_2 | \Phi_{\mu_0}^* \rangle = - \langle \hat{\sigma}_{i+1,\bar{a}}^x \rangle_{\mathbb{Z}_2}^{\text{I}}(t), \quad (\text{S61})$$

while the cross terms yield

$$\begin{aligned} \langle \hat{\sigma}_{i,a}^x \rangle_{\mathbb{Z}_2}^{\text{II}}(t) &= \sum_{\mu_0 \nu} \langle \Phi_{\mu_0} | \hat{\sigma}_{i,a}^x | E_\nu \rangle \langle E_\nu | \mathbb{Z}_2 \rangle \langle \mathbb{Z}_2 | \Phi_{\mu_0} \rangle e^{-iE_\nu t} \\ &= - \sum_{\mu_0 \nu} \langle \Phi_{\mu_0}^* | \hat{\sigma}_{i+1,\bar{a}}^x - E_\nu \rangle \langle -E_\nu | \mathbb{Z}_2 \rangle \langle \mathbb{Z}_2 | \Phi_{\mu_0}^* \rangle e^{-iE_\nu t} = - \langle \hat{\sigma}_{i+1,\bar{a}}^x \rangle_{\mathbb{Z}_2}^{\text{II}}(t). \end{aligned} \quad (\text{S62})$$

Moreover, the contribution from the non-zero sector is given by

$$\begin{aligned} \langle \hat{\sigma}_{i,a}^x \rangle_{\mathbb{Z}_2}^{\text{III}}(t) &= \sum_{\mu\nu} \langle E_\mu | \hat{\sigma}_{i,a}^x | E_\nu \rangle \langle E_\nu | \mathbb{Z}_2 \rangle \langle \mathbb{Z}_2 | \Phi_{\mu_0} \rangle e^{i(E_\mu - E_\nu)t} \\ &= - \sum_{\mu\nu} \langle -E_\mu | \hat{\sigma}_{i+1,\bar{a}}^x - E_\nu \rangle \langle -E_\nu | \mathbb{Z}_2 \rangle \langle \mathbb{Z}_2 | -E_\mu \rangle e^{i(E_\mu - E_\nu)t} = - \langle \hat{\sigma}_{i+1,\bar{a}}^x \rangle_{\mathbb{Z}_2}^{\text{III}}(t). \end{aligned} \quad (\text{S63})$$

Thus we finally obtain

$$\langle \hat{\sigma}_{i,a}^x \rangle_{\text{vac}}(t) = - \langle \hat{\sigma}_{i+1,\bar{a}}^x \rangle_{\mathbb{Z}_2}(t). \quad (\text{S64})$$

This concludes the derivation of the relations suggested by the numerical quench experiments for the $|\mathbb{Z}_2\rangle$ initial state.

Next, we consider the $|\text{vac}\rangle$ initial state. The computations are exactly similar to those for the $|\mathbb{Z}_2\rangle$ initial state. For the $\langle \sigma_i^z \rangle(t)$, we find, using \hat{C}_1 operator, for the zero-energy sector

$$\langle \hat{\sigma}_{i,a}^z \rangle_{\text{vac}}^{\text{I}}(t) = \sum_{\mu_0 \nu_0} \langle \Phi_{\mu_0} | \hat{\sigma}_{i,a}^z | \Phi_{\nu_0} \rangle \langle \Phi_{\nu_0} | \text{vac} \rangle \langle \text{vac} | \Phi_{\mu_0} \rangle = \sum_{\mu_0 \nu_0} \langle \Phi_{\mu_0}^* | \hat{\sigma}_{i+1,a}^z | \Phi_{\nu_0}^* \rangle \langle \Phi_{\nu_0}^* | \text{vac} \rangle \langle \text{vac} | \Phi_{\mu_0}^* \rangle = \langle \hat{\sigma}_{i+1,a}^z \rangle_{\text{vac}}^{\text{I}}(t). \quad (\text{S65})$$

The last equality in the above equation follows from the fact that $\{|\Phi_{\mu_0}\rangle\}$ and $\{|\Phi_{\mu_0^*}\rangle\}$ both form the zero energy degenerate subspace of $\hat{\mathcal{H}}$. Similarly, we can utilize $\hat{\mathcal{C}}_2$ operator ($|\Phi_{\mu_0^*}\rangle = \hat{\mathcal{C}}_2 |\Phi_{\mu_0}\rangle$) to find

$$\langle \hat{\sigma}_{i,a}^z \rangle_{\text{vac}}^{\text{I}}(t) = \sum_{\mu_0 \nu_0} \langle \Phi_{\mu_0} | \hat{\sigma}_{i,a}^z | \Phi_{\nu_0} \rangle \langle \Phi_{\nu_0} | = \langle \hat{\sigma}_{i+1,\bar{a}}^z \rangle_{\text{vac}}^{\text{I}}(t). \quad (\text{S66})$$

A similar relation can be worked out for the cross terms which connects the zero- and the non-energy sectors. Utilizing $\hat{\mathcal{C}}_1$ and \mathcal{C}_2 operators a similar straightforward calculations shows

$$\langle \hat{\sigma}_{i,a}^z \rangle_{\text{vac}}^{\text{II}}(t) = \langle \hat{\sigma}_{i+1,a}^z \rangle_{\text{vac}}^{\text{II}}(t) = \langle \hat{\sigma}_{i+1,\bar{a}}^z \rangle_{\text{vac}}^{\text{II}}(t), \quad (\text{S67})$$

while for terms within the non-zero energy sectors, we find

$$\langle \hat{\sigma}_{i,a}^z \rangle_{\text{vac}}^{\text{III}}(t) = \langle \hat{\sigma}_{i+1,a}^z \rangle_{\text{vac}}^{\text{III}}(t) = \langle \hat{\sigma}_{i+1,\bar{a}}^z \rangle_{\text{vac}}^{\text{III}}(t). \quad (\text{S68})$$

From these above relations, we can conclude that

$$\langle \hat{\sigma}_{i,a}^z \rangle_{\text{vac}}(t) = \langle \hat{\sigma}_{i+1,a}^z \rangle_{\text{vac}}(t) = \langle \hat{\sigma}_{i+1,\bar{a}}^z \rangle_{\text{vac}}(t). \quad (\text{S69})$$

This conforms to the numerical results and also implies that there is no imbalance for $|\sigma_{ia}^z\rangle(t)$ for the $|\text{vac}\rangle$ initial state.

Finally, we consider $\langle \hat{\sigma}_{i,a}^x \rangle_{\text{vac}}(t)$. The computations are exactly identical to those elaborated in the previous cases and we find

$$\langle \hat{\sigma}_{i,a}^x \rangle_{\text{vac}}(t) = -\langle \hat{\sigma}_{i+1,a}^x \rangle_{\text{vac}}(t) = -\langle \hat{\sigma}_{i+1,\bar{a}}^x \rangle_{\text{vac}}(t), \quad (\text{S70})$$

which conforms to the relation between the matrix elements found in the main text.

S6. FIDELITY AND SHANNON ENTROPY DYNAMICS FROM $|\mathbb{Z}_2\rangle$ AND $|\mathbb{Z}_3\rangle$ INITIAL STATES IN PXP CHAINS

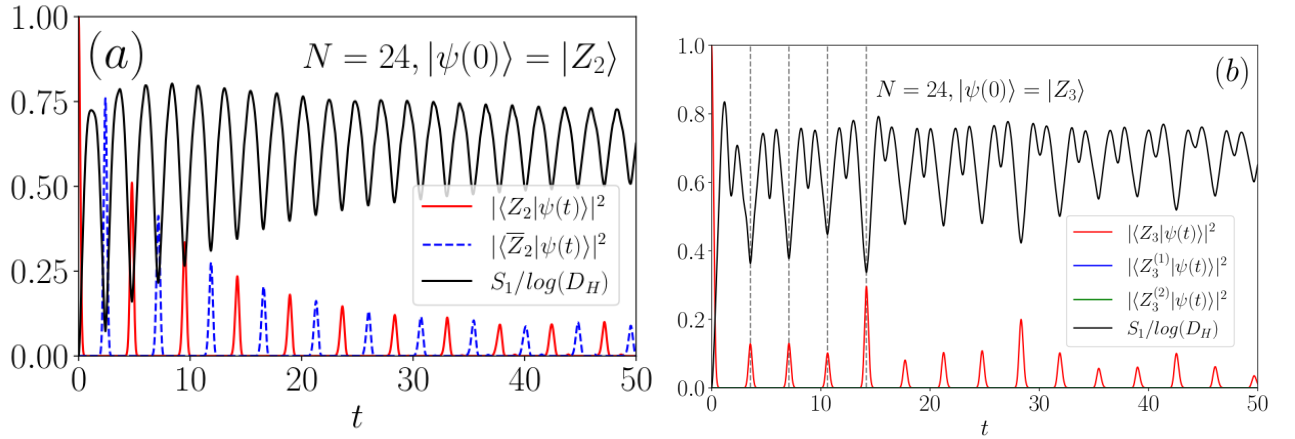


FIG. S5. (a) Plot of $|\langle \mathbb{Z}_2 | \psi(t) \rangle|^2$ (red), $|\langle \bar{\mathbb{Z}}_2 | \psi(t) \rangle|^2$ (dotted blue) and $S_1(t)$ (black) as a function of t for $|\psi(0)\rangle = |\mathbb{Z}_2\rangle$ in the PXP chain with $N = 24$ sites. (b) Plot of $|\langle \mathbb{Z}_3 | \psi(t) \rangle|^2$ (red), $|\langle \mathbb{Z}_3^{(1)} | \psi(t) \rangle|^2$ (blue), $|\langle \mathbb{Z}_3^{(2)} | \psi(t) \rangle|^2$ (green) and $S_1(t)$ (black) as a function of t for $|\psi(0)\rangle = |\mathbb{Z}_3\rangle$ in the PXP chain with $N = 24$ sites.

In PXP chains (Eq. 1 of main text with $\Delta = 0$ on a 1D chain with PBC), both period-2 $|\mathbb{Z}_2\rangle$ as well as period-3 $|\mathbb{Z}_3\rangle$ initial Fock states lead to persistent many-body revivals in $\mathcal{F}(t)$ though the latter state gives weaker revivals (Fig. S5). The Shannon entropy $S_1(t)$ shows local minima at the same times as the maxima in $\mathcal{F}(t)$ in both cases. Importantly, $S_1(t)$ shows additional pronounced local minima at times which are equidistant between two consecutive fidelity revivals in both the cases. While these additional local minima in $S_1(t)$ can be correlated to the appearance of local maxima of $|\langle \bar{\mathbb{Z}}_2 | \psi(t) \rangle|^2$ where $|\bar{\mathbb{Z}}_2\rangle$ refers to the translated partner of $|\mathbb{Z}_2\rangle$ (Fig. S5 (a)), the case with $|\mathbb{Z}_3\rangle$ is more complicated (Fig. S5 (b)). These additional local minima in $S_1(t)$ cannot be explained as revivals in either $|\langle \mathbb{Z}_3^{(1)} | \psi(t) \rangle|^2$ or $|\langle \mathbb{Z}_3^{(2)} | \psi(t) \rangle|^2$, where $|\mathbb{Z}_3^{(1)}\rangle$ and $|\mathbb{Z}_3^{(2)}\rangle$ refer to the two translated partners of $|\mathbb{Z}_3\rangle$ (Fig. S5 (b)). Nonetheless, the additional minima in $S_1(t)$ still suggests that the other end state has a natural representation in terms of the superposition of a small number of Fock states, when starting from an initial $|\mathbb{Z}_3\rangle$ Fock state.

S7. PXP AND NON-PXP REGIMES OF MANY-BODY REVIVALS IN LADDERS

In Fig. S6 (a) and Fig. S6 (b), we show the time evolution of the following fidelities, $|\langle \mathbb{Z}_2 | \psi(t) \rangle|^2$ and $|\langle \bar{\mathbb{Z}}_2 | \psi(t) \rangle|^2$, respectively, where $|\psi(0)\rangle = |\mathbb{Z}_2\rangle$ and $N = 32$ for various values of $\Delta \leq 0.25$. We dub this as the ‘‘PXP regime’’ where only the $|\mathbb{Z}_2\rangle$ and its particle-hole symmetric partner $|\bar{\mathbb{Z}}_2\rangle$ show periodic revivals. While the Shannon entropy S_1 shows local minima at the same times as the local maxima in $|\langle \mathbb{Z}_2 | \psi(t) \rangle|^2$ (see Fig. 4(a) in main text), S_1 also displays additional local minima (see Fig. 4(a) in main text) which can be correlated with $|\langle \bar{\mathbb{Z}}_2 | \psi(t) \rangle|^2$ attaining local maxima.

On the other hand, these additional local minima in S_1 are entirely absent (see Fig. 4(b) in main text) in the non-PXP like scarring regime from $|\psi(0)\rangle = |\mathbb{Z}_2\rangle$ where the dips in S_1 correspond only to the local maxima in the fidelity $|\langle \mathbb{Z}_2 | \psi(t) \rangle|^2$ where $|\psi(0)\rangle = |\mathbb{Z}_2\rangle$ and $N = 32$ for various values of $\Delta \geq 0.70$ (Fig. S6 (c)). Similar non-PXP like scarring is also observed starting from the $|\text{vac}\rangle$ state (see Fig. 4(c) in main text) where the dips in S_1 correspond only to the local maxima in the fidelity $|\langle \text{vac} | \psi(t) \rangle|^2$ for $N = 32$ for various values of $\Delta \geq 0.70$ (Fig. S6 (d)).

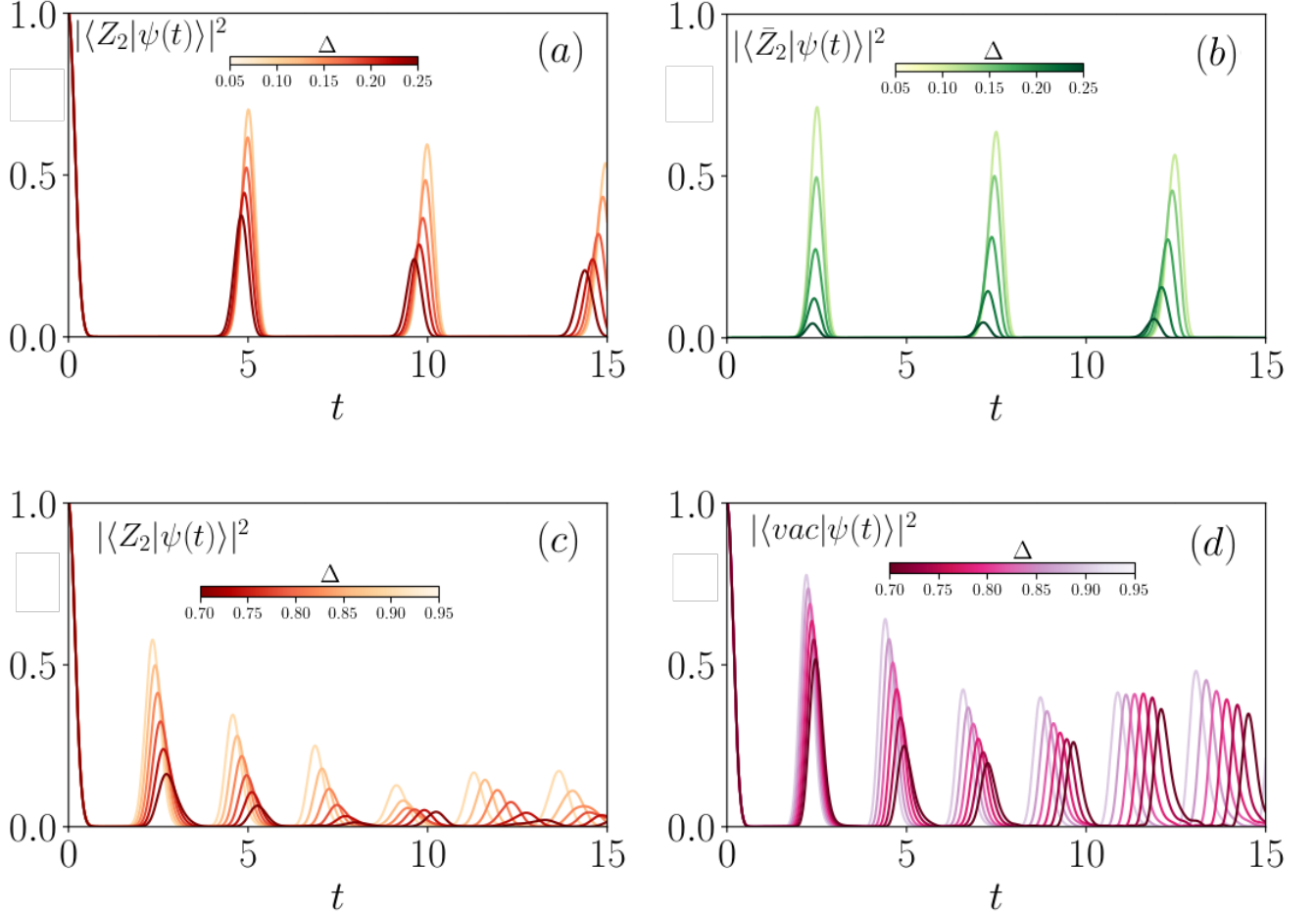


FIG. S6. Plot of (a) $|\langle \mathbb{Z}_2 | \psi(t) \rangle|^2$ and (b) $|\langle \bar{\mathbb{Z}}_2 | \psi(t) \rangle|^2$ as a function of t for $|\psi(0)\rangle = |\mathbb{Z}_2\rangle$ in the PXP regime. (c) Plot of $|\langle \mathbb{Z}_2 | \psi(t) \rangle|^2$ as a function of t for initial state $|\psi(0)\rangle = |\mathbb{Z}_2\rangle$ in the non-PXP regime. (d) Plot of $|\langle \text{vac} | \psi(t) \rangle|^2$ as a function of t for initial state $|\psi(0)\rangle = |\text{vac}\rangle$ in the non-PXP regime. In all panels, various values of Δ are displayed using a color bar in the inset of each corresponding panel. For all plots $N = 32$ and $w = \hbar = 1$.

It is clarifying to monitor the dynamics of the bipartite entanglement entropy as a function of time in the non-PXP regime. We can define two distinct partitions which we refer to as \parallel [Fig. S7 (a)] (\perp) [Fig. S7 (b)] where the partition is chosen to be parallel (perpendicular) to the legs of the ladder which divides the system into two equal halves. Next, we calculate the reduced density matrix of any of the subsystems by integrating out the degrees of freedom in the other subsystem, which gives

$$\rho_{A(B)}(t) = \text{Tr}_{B(A)} \rho_{AB}(t) \quad (\text{S71})$$

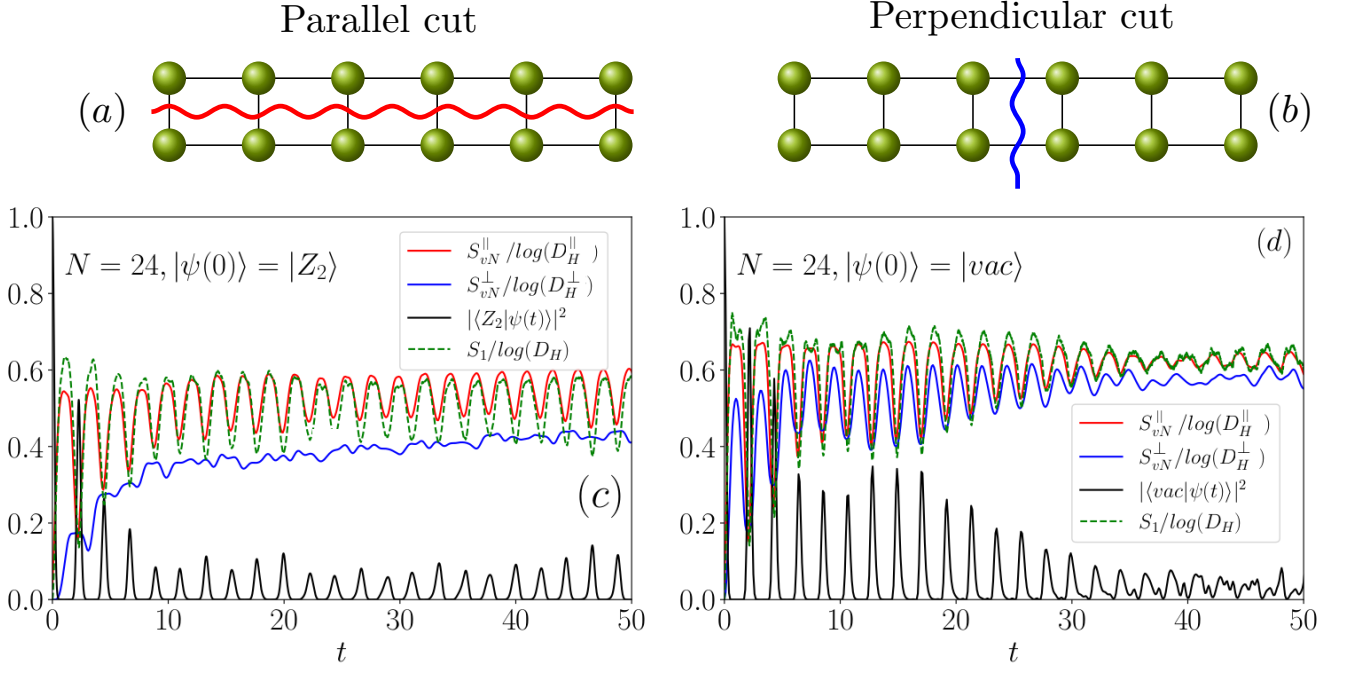


FIG. S7. The bipartitions used to calculate S_{vN}^{\parallel} shown in (a) and S_{vN}^{\perp} shown in (b). The time evolution of the Shannon entropy $S_1/\log(\mathcal{D}_H)$ (dotted green), fidelity $\mathcal{F}(t)$ (black), as well as the bipartite entanglement entropies $S_{vN}^{\parallel}/\log(\mathcal{D}_H^{\parallel})$ (red), $S_{vN}^{\perp}/\log(\mathcal{D}_H^{\perp})$ (blue) shown for $|Z_2\rangle$ (c) and $|vac\rangle$ (d) initial states for a ladder with $N = 24$ sites and $\Delta = 1$.

where $\rho_{AB}(t) = |\psi(t)\rangle\langle\psi(t)|$ refers to the full density matrix, and A, B refer to the two subsystems. From this, the entanglement entropy can be computed by using $S_{vN}^{\parallel/\perp}(t) = -\text{Tr}(\rho_{\parallel/\perp}(t)\log(\rho_{\parallel/\perp}(t)))$ where \parallel/\perp refers to the appropriate bipartition. We show the time evolution of $S_{vN}^{\parallel}/\log(\mathcal{D}_H^{\parallel})$, $S_{vN}^{\perp}/\log(\mathcal{D}_H^{\perp})$ and $S_1/\log(\mathcal{D}_H)$ starting from a $|Z_2\rangle$ (Fig. S7 (c)) as well as $|vac\rangle$ (Fig. S7 (d)) initial state for a ladder with $N = 24$ sites for $\Delta = 1$ using ED. Here, while \mathcal{D}_H refers to the full Hilbert space dimension, $\mathcal{D}_H^{\parallel/\perp}$ refers to the Hilbert space dimension of a subsystem after performing the trace over the other subsystem. For $N = 24$, $\mathcal{D}_H = 710647$, $\mathcal{D}_H^{\parallel} = 2207$, and $\mathcal{D}_H^{\perp} = 1393$. In both cases, $S_{vN}^{\parallel}/\log(\mathcal{D}_H^{\parallel})$ mimics the behavior of $S_1(t)$ and displays local maxima at times that are equidistant between the consecutive local maxima of $\mathcal{F}(t)$. This suggests that the other end state may be approximated in a simpler manner in a basis composed of entangled spins along rungs rather than in an unentangled Fock basis. While $S_{vN}^{\perp}/\log(\mathcal{D}_H^{\perp})$ is relatively featureless in Fig. S7 (c), it behaves similar to $S_{vN}^{\parallel}/\log(\mathcal{D}_H^{\parallel})$ in Fig. S7 (d), highlighting the different origin of the revivals in the non-PXP regime starting from a Néel and a vacuum initial state, respectively.

S8. OVERLAP OF MANY-BODY EIGENSTATES WITH $|Z_2\rangle$ AND $|vac\rangle$

In Fig. S9 (a),(b),(c), we show the time period of fidelity revivals. The time period of revivals as denoted in the inset by $\tau_{\mathcal{F}}$ is computed as the difference in times of first and second revivals. i.e. $\tau_{\mathcal{F}} = t_2 - t_1$. This time period corresponds to a frequency shown as $\Omega_{\mathcal{F}} = 2\pi/(t_2 - t_1)$, which in all cases is very close to the energy of the first non-zero energy QMBS, E_* , as shown in Fig. S8 by solid gray lines.

In Fig. S10 (a),(b),(c), we show the time period of oscillations of longitudinal magnetization. This time period, as denoted in the inset by τ_{M_z} is computed as the difference in times of first and second revivals. i.e. $\tau_{M_z} = t_2 - t_1$. This time period corresponds to a frequency shown as $\Omega_{M_z} = 2\pi/(t_2 - t_1)$, which in case (a) is very close to twice of the energy of the first non-zero energy QMBS, E_* , as shown in Fig. S10 by solid gray lines. In other cases i.e. (b) and (c) the frequency of oscillations Ω_{M_z} is equal to E_* .

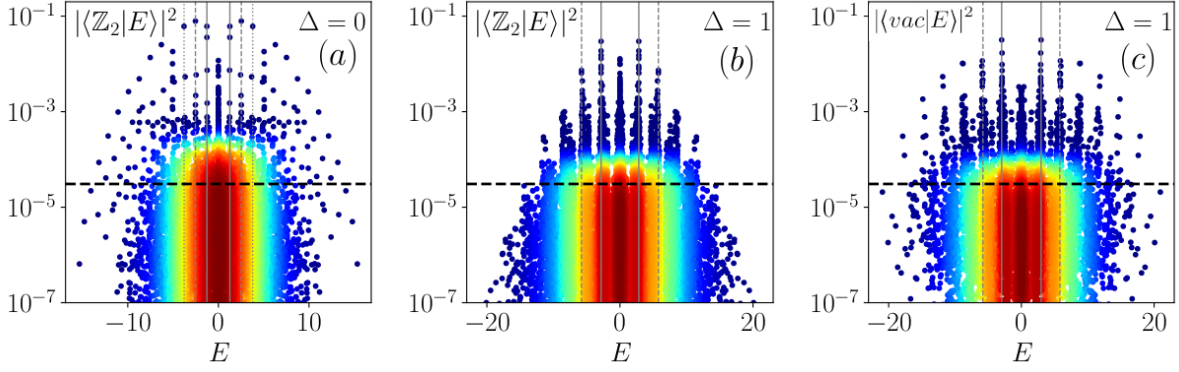


FIG. S8. Plot of overlap of many-body eigenstates of $N = 28$ ladder in $k_x = 0$ sector with specific Fock states (a) $|\langle \mathbb{Z}_2 | E \rangle|^2$ for $\Delta = 0$, (b) $|\langle \mathbb{Z}_2 | E \rangle|^2$ for $\Delta = 1$ and (c) $|\langle \text{vac} | E \rangle|^2$ for $\Delta = 1$. For all plots $w = \hbar = 1$ and the color scheme indicates higher overlap for warmer colors.

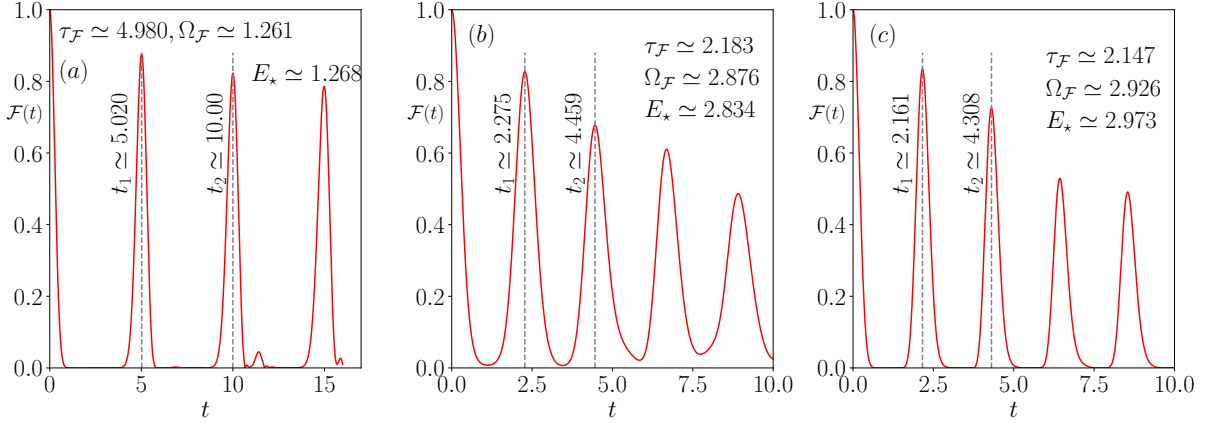


FIG. S9. Plot of the fidelity $\mathcal{F}(t)$ as a function of t showing time periods of fidelity revivals for (a) $\Delta = 0, |\psi(0)\rangle = |\mathbb{Z}_2\rangle$, (b) $\Delta = 1, |\psi(0)\rangle = |\mathbb{Z}_2\rangle$ and (c) $\Delta = 1, |\psi(0)\rangle = |\text{vac}\rangle$. For all plots $N = 28$ and $w = \hbar = 1$.

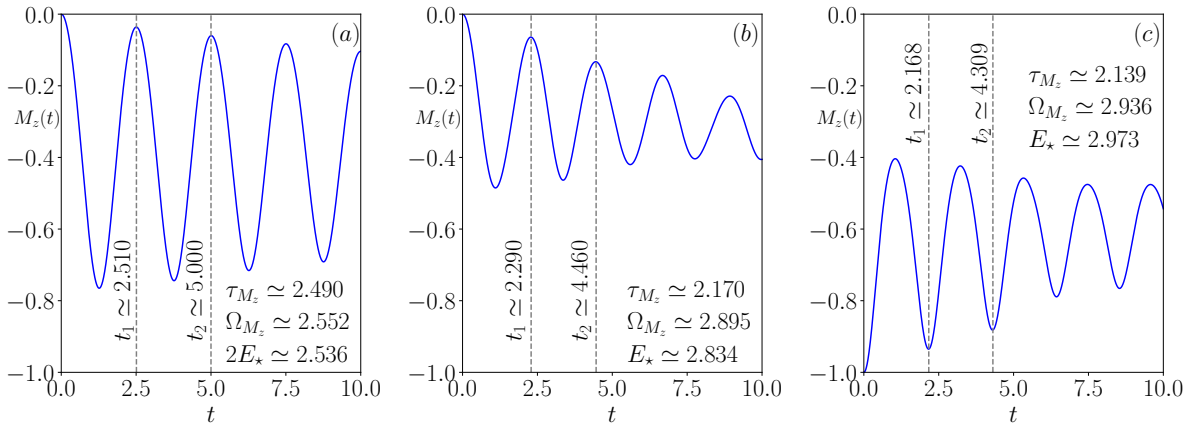


FIG. S10. Plot of the longitudinal magnetization density as a function of t for (a) $\Delta = 0, |\psi(0)\rangle = |\mathbb{Z}_2\rangle$, (b) $\Delta = 1, |\psi(0)\rangle = |\mathbb{Z}_2\rangle$ and (c) $\Delta = 1, |\psi(0)\rangle = |\text{vac}\rangle$.